Draft version December 6, 2017
Typeset using LaTeX **twocolumn** style in AASTeX61

THE *HERSCHEL*-ATLAS DATA RELEASE 2, PAPER I. SUBMILLIMETRE AND FAR-INFRARED IMAGES OF THE SOUTH AND NORTH GALACTIC POLES: THE LARGEST *HERSCHEL* SURVEY OF THE EXTRAGALACTIC SKY

Matthew W. L. Smith,[1] Edo Ibar,[2] Steve J. Maddox,[1,3] Elisabetta Valiante,[1] Loretta Dunne,[1,3] Stephen Eales,[1] Simon Dye,[4] Christina Furlanetto,[4] Nathan Bourne,[3] Phil Cigan,[1] Rob J. Ivison,[3,5] Haley Gomez,[1] Daniel J. B. Smith,[6] and Sébastien Viaene[7,6]

[1] *School of Physics & Astronomy, Cardiff University, The Parade, Cardiff, CF24 3AA, UK.*
[2] *Instituto de Física y Astronomía, Universidad de Valparaíso, Avda. Gran Bretaña 1111, Valparaíso, Chile.*
[3] *Institute for Astronomy, The University of Edinburgh, Royal Observatory, Blackford Hill, Edinburgh, EH9 3HJ, UK.*
[4] *School of Physics and Astronomy, University of Nottingham, University Park, Nottingham, NG7 2RD, UK.*
[5] *European Southern Observatory, Karl-Schwarzschild-Strasse 2, D-85748, Garching, Germany.*
[6] *Centre for Astrophysics Research, School of Physics Astronomy and Mathematics, University of Hertfordshire, College Lane, Hatfield, Hertfordshire, AL10 9AB, UK.*
[7] *Sterrenkundig Observatorium, Universiteit Gent, Krijgslaan 281, B-9000 Gent, Belgium.*

(Received July 3, 2017; Accepted November 14, 2017)

Submitted to ApJS

ABSTRACT

We present the largest submillimeter images that have been made of the extragalactic sky. The *Herschel* Astrophysical Terahertz Large Area Survey (*H*-ATLAS) is a survey of 660 deg^2 with the PACS and SPIRE cameras in five photometric bands: 100, 160, 250, 350, and 500μm. In this paper we present the images from our two largest fields which account for $\sim$75% of the survey. The first field is 180.1 deg^2 in size centered on the North Galactic Pole (NGP) and the second field is 317.6 deg^2 in size centered on the South Galactic Pole. The NGP field serendipitously contains the Coma cluster. Over most ($\sim$80%) of the images, the pixel noise, including both instrumental noise and confusion noise, is approximately 3.6, and 3.5 mJy pix^{-1} at 100 and 160μm, and 11.0, 11.1 and 12.3 mJy beam^{-1} at 250, 350 and 500μm, respectively, but reaches lower values in some parts of the images. If a matched filter is applied to optimize point-source detection, our total 1σ map sensitivity is 5.7, 6.0, and 7.3 mJy at 250, 350, and 500μm, respectively. We describe the results of an investigation of the noise properties of the images. We make the most precise estimate of confusion in SPIRE maps to date finding values of 3.12 ± 0.07, 4.13 ± 0.02 and 4.45 ± 0.04 mJy beam^{-1} at 250, 350, and 500μm in our un-convolved maps. For PACS we find an estimate of the confusion noise in our fast-parallel observations of 4.23 and 4.62 mJy beam^{-1} at 100 and 160μm. Finally, we give recipes for using these images to carry out photometry, both for unresolved and extended sources.

Keywords: surveys - cosmology: observations - submillimetre: galaxies - galaxies: statistics - methods: data analysis

1. INTRODUCTION

This is the first of three papers describing the second major data release of the *Herschel* Astrophysical Terahertz Large Area Survey (*Herschel*-ATLAS or *H*-ATLAS), the largest single key project carried out in open time with the *Herschel Space Observatory* (Pilbratt et al. 2010). The *H*-ATLAS is a survey of approximately 660 deg^2 of sky in five photometric bands: 100, 160, 250, 350, and 500μm (Eales et al. 2010). Although the original goal of the survey was to study dust, and the newly formed stars hidden by dust, in galaxies in the

Corresponding author: Matthew W. L. Smith
Matthew.Smith@astro.cf.ac.uk

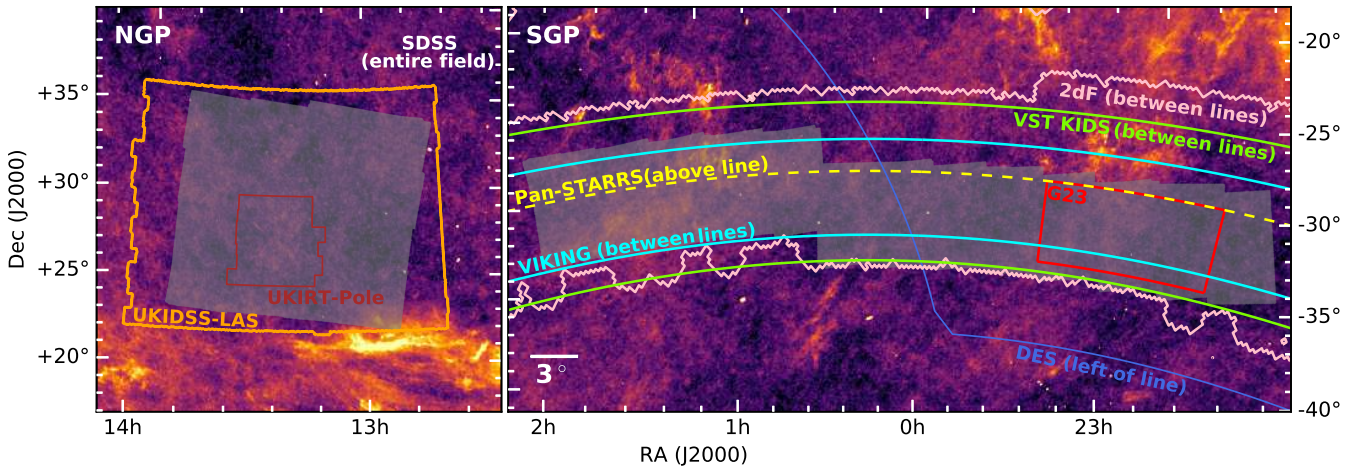

Figure 1. Overlapping, coverage of surveys in the NGP and SGP fields. The figure shows a 350μm map from *Planck* (color-image) for both fields (with the same angular scale), with the gray regions illustrating the coverage of the *H*-ATLAS observations. The regions observed in complementary surveys are shown by the colored lines. In the NGP field, the entire *H*-ATLAS region is observed by the UKIDSS-Large Area Survey and the SDSS, as well as the UKIRT-Pole survey which covers 14% of the *H*-ATLAS NGP field. In the SGP there is overlapping coverage with the GAMA-23 hr field, VST-KIDS, VIKING, DES, Pan-STARRS and 2dF each with 18%, 98%, 79%, 24%, 50% and 99% overlap with *H*-ATLAS, respectively. For details of these surveys see Section 1

nearby ($z < 0.4$) universe (Dunne et al. 2011; Eales et al. 2017), in practice the exceptional sensitivity of *Herschel*, aided by the large negative *k*-correction at submillimeter wavelengths (Blain & Longair 1993), has meant that the median redshift of the sources detected in the survey is $\simeq$1 (Pearson et al. 2013). The survey has therefore also already proved useful for astronomers interested in studying galaxies in the early universe (e.g. Lapi et al. 2011) and also as a rich source of high-redshift galaxies, both objects that are lensed (Negrello et al. 2010, 2017; González-Nuevo et al. 2012) and those that which are unlensed (Ivison et al. 2016; Oteo et al. 2016). The large area of the survey and the high Galactic latitude of the fields also mean that it can potentially be used to look for Galactic objects with very low dust masses (Eales et al. 2010; Thompson et al. 2010).

The five *H*-ATLAS fields were selected to be areas with relatively little emission from dust in the Milky Way, as judged from the IRAS 100μm images (Neugebauer et al. 1984), and with a large amount of data in other wavebands. In 2010 for the Science Demonstration Phase (SDP) of *Herschel*, we released one 16 deg^2 field in the GAMA 9 hr field (Ibar et al. 2010; Pascale et al. 2011; Rigby et al. 2011; Smith et al. 2011). Our first data release included three fields on the celestial equator centred at approximately 9, 12, and 15 hr (Bourne et al. 2016; Valiante et al. 2016). These three fields, which cover 161 deg^2 constitute $\sim$ 25% of the *H*-ATLAS survey, are rich in multi-wavelength data and in particular are covered by the Sloan Digital Sky Survey (SDSS; Abazajian et al. 2009), the VST Kilo-Degree Survey (KIDS; de Jong et al. 2013), the VISTA Kilo-Degree Infrared Galaxy Survey (VIKING; Edge et al. 2013), the 2-Degree-Field Galaxy Redshift Survey (2dF; Colless et al. 2001), and the Galaxy and Mass Assembly project (GAMA; Driver et al. 2009; Liske et al. 2015). The data we released for these fields consisted of the *Herschel* images and catalogs of the 120,230 *Herschel* sources and of 44,835 optical counterparts to these sources.

Our second data release is for the two larger fields at the north and south Galactic poles (NGP and SGP). The NGP field is centered approximately at R.A. of 13^h 18^m and a decl. of +29° 13′ (J2000) and has an area of 180.1 deg^2. The field is covered by the SDSS and has near-infrared coverage from the UKIRT Infrared Deep Sky Survey Large Area Survey (Lawrence et al. 2007). The *H*-ATLAS team itself also used UKIRT to carry out a deep *K*-band survey of part of the field (UKIRT Pole Survey), covering 25.93 deg^2 (Paper III; Furlanetto et al. 2017). The NGP field contains the Coma cluster, and the *Herschel* images have been used to study the dust in the cluster galaxies (Fuller et al. 2016).

The SGP field is centered approximately at a R.A. of 0^h 6^m and a decl. of -32° 44′ (J2000) and has an area of 317.6 deg^2. The field was covered by the 2dF spectroscopic survey and has been imaged in four optical bands (u, g, r and i) as part of KIDS, and in five near-infrared bands (Z, Y, J, H and K_s) as part of the VIKING. The *H*-ATLAS data also cover the GAMA G23 field and has some overlap with the Dark Energy Survey (Dark Energy Survey Collaboration et al. 2016), and Pan-STARRS (Chambers et al. 2016). Figure 1

shows the regions where complementary surveys overlap with the NGP and SGP fields.

Our data release for the *H*-ATLAS survey of the NGP and SGP is described in three papers. In this paper, we describe the *Herschel* images and an investigation of their statistical properties. We also give enough information for the astronomical community to be able to use these images to carry out reliable photometry of individual objects and statistical 'stacking' analyses of classes of object. The second paper (Maddox et al. 2017) describes the catalogs of submillimeter sources found on the images. The third paper (Furlanetto et al. 2017) describes a search for the optical/near-infrared counterparts to the *Herschel* sources in the NGP field and the resulting multi-wavelength catalogue. All the images described in this paper are available from `www.h-atlas.org`, and Appendix A provides a guide to the products available, with a short description.

2. OBSERVING STRATEGY

We observed the NGP and SGP using the same *Herschel* observing mode as we used for the smaller fields on the celestial equator: the SPIRE-PACS parallel mode in which both the SPIRE (Griffin et al. 2010) and PACS (Poglitsch et al. 2010) instruments are used simultaneously. To maximise the area covered, and reduce potential $1/f$ noise, we used the fastest scan speed of $60\,\mathrm{arcsec\,s^{-1}}$ ($1/f$ noise or "low frequency noise" in bolometer timelines would lead to stripe artefacts in the map). Due to the offset between the cameras in the *Herschel* focal plane, the PACS and SPIRE images are offset by $\sim 22'$, which means a tiny fraction (4%) of both fields has data taken with only one camera. We observed both fields at 100 and 160μm with PACS and 250, 350, and 500μm with SPIRE.

An observation consists of "scan legs" where the telescope is moving at a constant velocity along a great circle across the field. At the end of each scan leg, the telescope decelerates and then moves a constant distance in an orthogonal direction to the beginning of the next scan leg, and then scans backwards across the field. The total area covered by an observation is therefore built up by combining a large number of scan legs during which the telescope is moving at a constant speed. Useful instrumental data is still being taken during the sections between scan legs and when the telescope is accelerating, but in the *H*-ATLAS SPIRE maps these "turn around" data are not included in the final maps. In parallel mode, the scan legs were separated by 155 arcsec in order to achieve a good coverage with both PACS and SPIRE. More details can be found in the SPIRE and PACS Observers' Manuals, which are available at `http://herschel.esac.esa.int`.

For all *H*-ATLAS fields our observing strategy was to ensure all locations were covered by two observations of each field with roughly orthogonal scan directions. The scans needed to be roughly orthogonal because a major concern before launch was that drifts in the bolometer signals of the instruments would lead to artefacts on the images with large angular scale. Obtaining observations with orthogonal scan directions makes it possible, with the correct map-making algorithm, to ensure that the final map does not contain any of these artefacts (Waskett et al. 2007). In practice, SPIRE, although not PACS, proved sufficiently stable that it was possible to remove any drifts that did occur using information from the thermistors attached to the bolometer arrays (Section 3.1), and even maps made from single observations were generally free of these artefacts. For PACS one of these advanced map-making algorithms is required; for details of the procedure we use see Section 4.

For the fields on the celestial equator, we followed this strategy by carrying out two observations with roughly orthogonal scan directions, each with an exposure time of roughly nine hours and generally one after the other. A pair of observations would cover a square area, or "tile", of side 4 degrees. Each of the equatorial fields was covered by four of these tiles (Valiante et al. 2016, hereafter V16). It was not possible to follow this simple procedure for the NGP and the SGP because of the need to obtain uniform sensitivity over such large fields and the sheer difficulty of scheduling such a large programme during a three-year mission with all the geometric constraints on the pointing and scanning directions set by the positions of the Sun and the Earth (Waskett et al. 2007). Instead, for the NGP and SGP, we constructed the survey out of much bigger tiles, with each tile being constructed out of two pairs of observations of rectangular regions of sky, with the long axes (and scan directions) of the observations in each pair being roughly parallel to each other and roughly orthogonal to the long axes of the observations in the other pair. The individual observations in the NGP typically had an observing time of $\sim$9.3–10.0 hr.

The top right-hand panels of Figures 2 and 3 show our scanning strategy for the NGP, which was covered by four of these large tiles. Each tile is almost a square with sides of $\simeq 7.2°$and $\simeq 6.5°$. Given the scheduling constraints, it was not possible to make all the tiles line up precisely, and to ensure complete coverage of each field, we made the tiles overlap slightly. The entire area covered by our observations is roughly a rectangle with dimensions of $\simeq 14.0°$by $\simeq 12.8°$. The area of the field

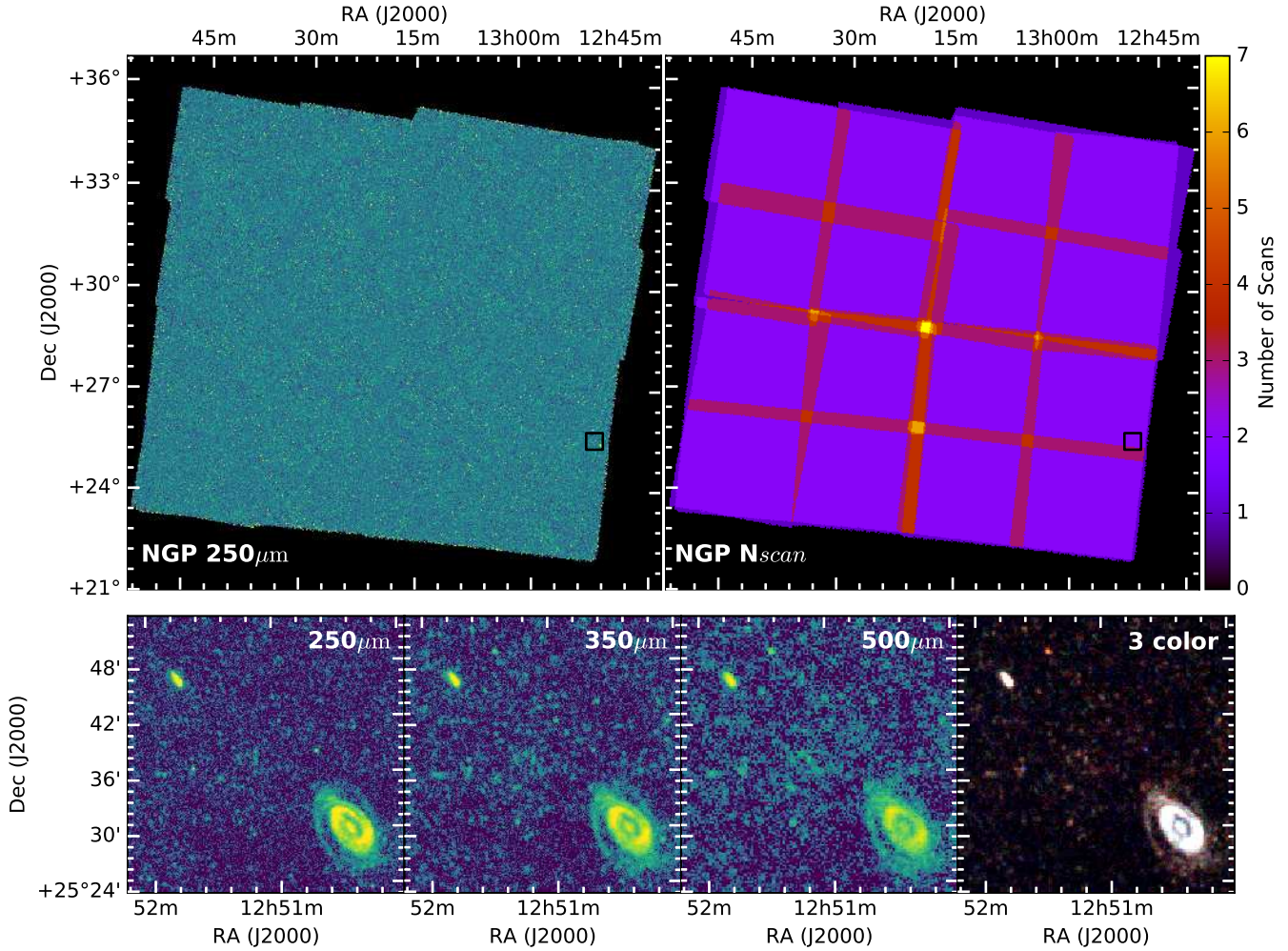

Figure 2. SPIRE maps of the NGP field. The larger top panels show the 250μm map *(left)* and the number of individual observations (N_{scan}) from which the map was constructed *(right)*. The row of lower panels show a close-up of a region centred on $\sim 13^h18^m$,29°18′, which is shown by the black rectangle in the top panels. The first three of the lower panels show the images at the three SPIRE wavelengths. The final panel shows an image formed by combining the three SPIRE images. On this three-color image, red shows sources that are brighter at 500μm and blue shows sources that are brighter at 250μm. Red sources will either be low-redshift galaxies with very cold dust or high-redshift galaxies. This region was not chosen at random and contains two local galaxies and a bright high-redshift lensed source (the red source at the top of the three-color image).

with useful data is 180.1 deg^2. The figures show the number of observations at each point for SPIRE (Figure 2) and PACS (Figure 3). They show that the design of our observing programme was quite successful, since most of the NGP has data from two roughly orthogonal observations, with narrow strips having data from four observations (and thus an increase in sensitivity), and with a few very small areas having data from even more observations and thus even better sensitivity.

For the SGP, we adopted the same procedure of creating roughly square tiles out of two pairs of parallel rectangles. The design of the survey is shown in the center panels of Figures 4 and 5, which show the coverage of SPIRE and PACS, respectively. The tiles form two rough rectangles which are touching but offset from each other. The shape of the SGP field is different from the one we envisioned before launch (Eales et al. 2010); the new design maximizes the overlap with the 2dF spectroscopic survey and the new spectroscopic survey carried out by the GAMA team at an R.A. of $\simeq 23^h$. The area of the field with useful data is 317.6 deg^2. The individual observations in the SGP had a typical exposure time of $\sim$9.3–10.1 hr.

The shape and size of the SGP field means that the tiles do not line up so well as for the NGP, therefore the coverage is slightly less uniform (Figures 4 and 5). The coverage was also less uniform due to two complications. The first was that during *Herschel* observation 1342196626 a planet (either Jupiter or Uranus) was at a position where light from it was reflected by the sup-

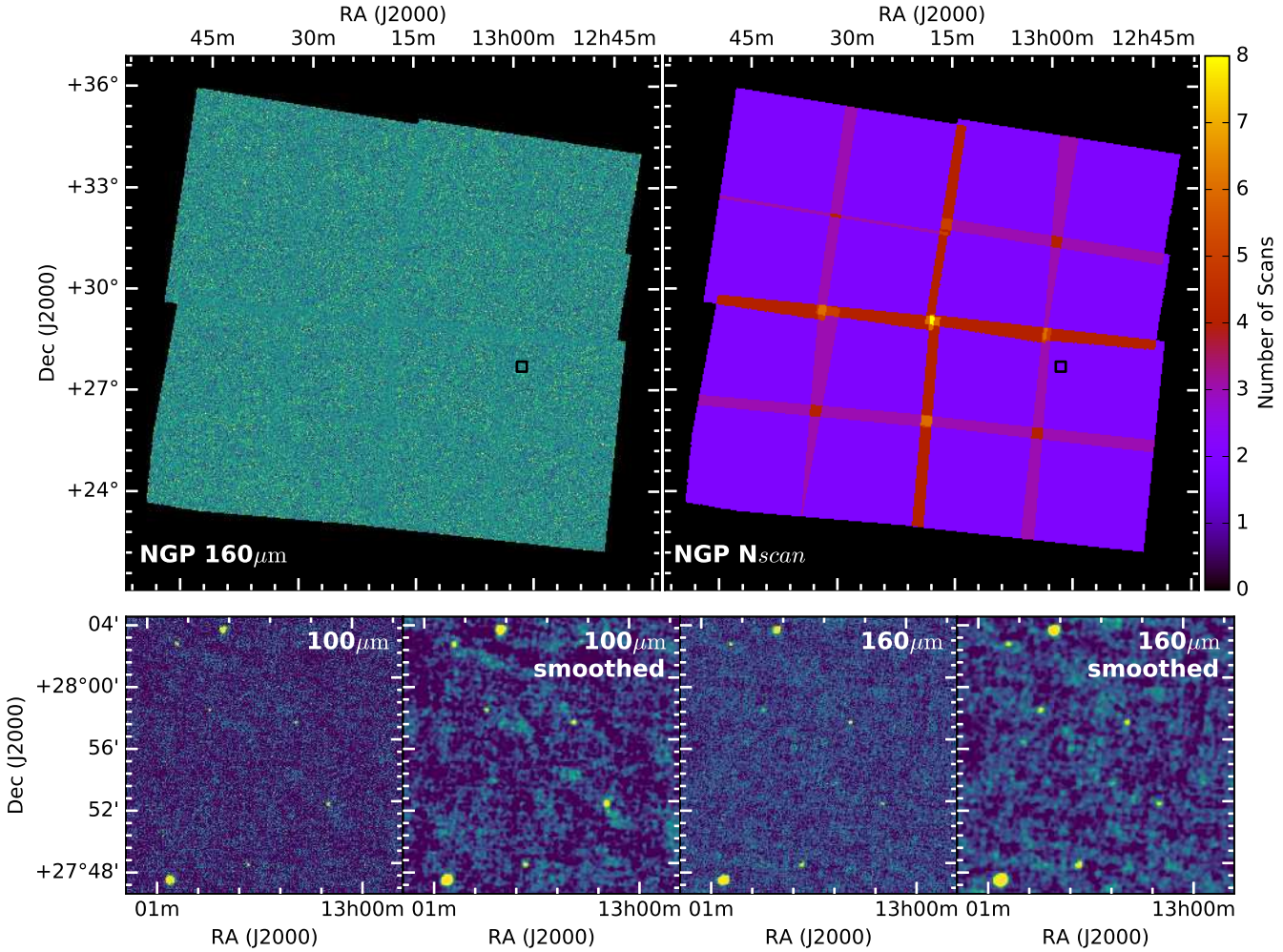

Figure 3. PACS maps of the NGP field. The larger top panels show the 160μm map *(left)* and the number of individual observations (N_{scan}) from which the map was constructed *(right)*. The row of lower panels show a small region of the Coma cluster at $\sim 13^h00^m$, $27°55'$ (shown by the black rectangle on the top panels) at both PACS wavelengths, both the raw images and images smoothed by a Gaussian with same full-width at half maximum as the point-spread function.

port structure of the secondary mirror into the SPIRE instrument, leading to a 'stray-light' feature on the image. After we discovered this feature, the *Herschel Science Centre* scheduled a replacement observation (obsid: 1342245911) covering an area $\simeq 1.8° \times 1.7°$ in size to patch the image. The patch can be seen in Figure 4 at R.A. $\sim 0^h16^m$, decl. $\simeq -32°43'$.

The second complication is that occasionally during our observations the SPIRE instrument went into safe mode, probably because it was hit by a cosmic ray, while PACS kept on observing. As a result, there is a region ($\sim 6.0° \times 3.5°$) at the western end of the SGP for which we have only one observation at each point for SPIRE (Figure 4) but the normal coverage with PACS (Figure 5); we were not able to obtain a replacement SPIRE observation because we ran out of allocated observing time. There are also two regions where we did succeed in getting replacement observations with SPIRE, and as a result we have better than the usual coverage with PACS. These regions are both toward the western end of the image (Figure 5). One is $\sim 6.0° \times 3.5°$ in area, for which at most points we have four observations rather than the usual two, and the other is a region $\sim 6.2° \times 3.5°$ in size, for which at most points we have three observations rather than the usual two.

3. THE SPIRE OBSERVATIONS

H-ATLAS imaged the sky with the SPIRE camera simultaneously through three submillimeter filters centered at 250, 350 and 500μm. Each filter was approximately 30% wide in $\Delta\lambda/\lambda$. A full description of the instrument is in Griffin et al. (2010). We have given a very detailed description of the data reduction below in order to make clear the differences in the procedure for the NGP and SGP fields to those used for the fields

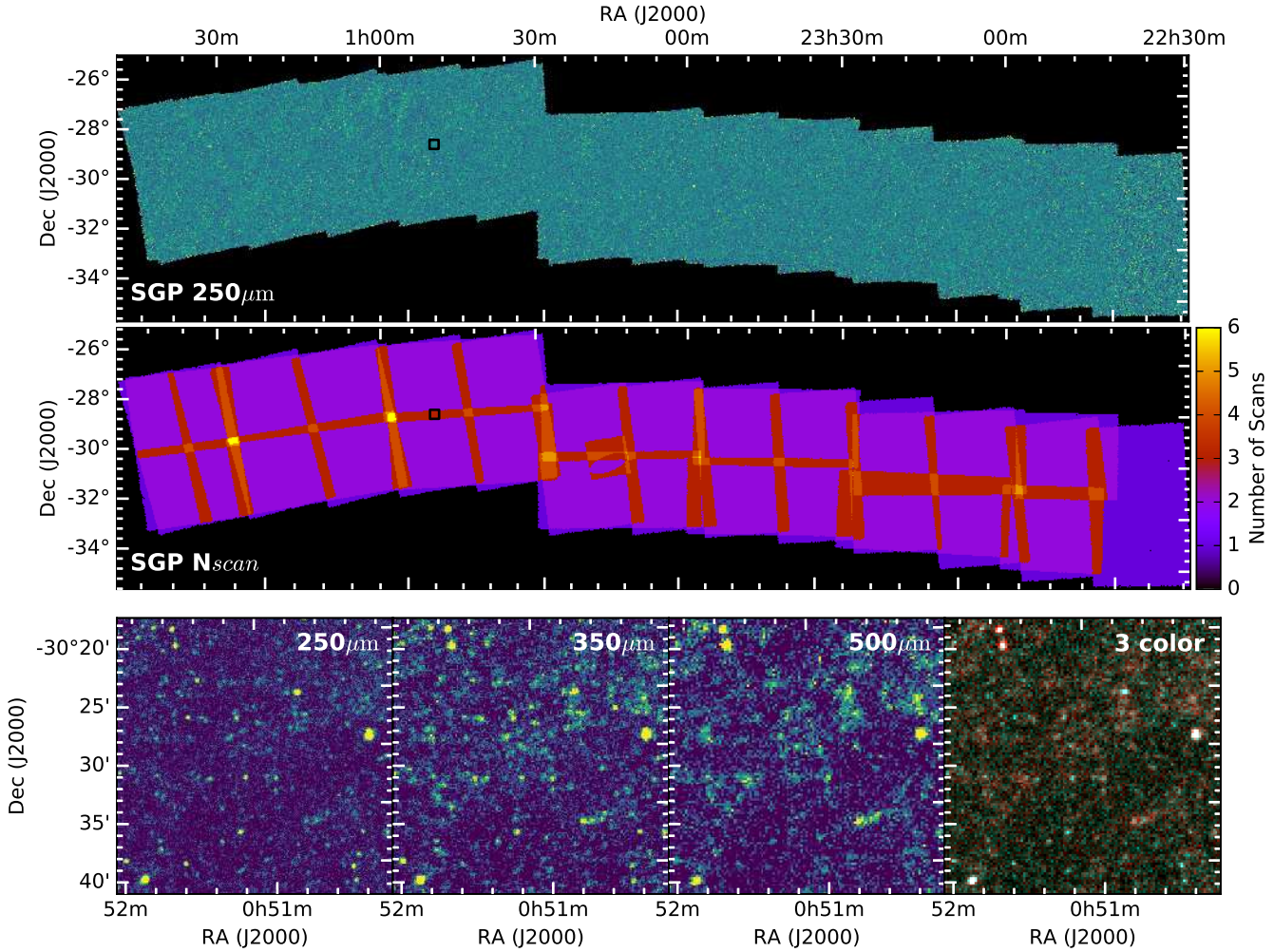

Figure 4. SPIRE maps of the SGP field. The larger top panels show the 250μm map *(top)* and the number of observations (N_{scan}) from which the map was made *(middle)*. Note the region at the western edge of the field where the map was made from only a single observation (see the text). The row of lower panels show a close-up of a region centered on $\sim 0^h51^m$, -30°30′, which is shown by the black rectangle on the top panels. The first three of the lower panels show the images at the at the three SPIRE wavelengths. The final panel shows an image formed by combining the three SPIRE images. On this three-color image, red shows sources that are brighter at 500μm and blue shows sources that are brighter at 250μm. Red sources will either be low-redshift galaxies with very cold dust or high-redshift galaxies.

on the celestial equator (V16) and from the procedures used for other *Herschel* surveys.

In Section 3.1 we describe our treatment of the SPIRE timelines from the raw data to reduced timelines. In Section 3.2 we discuss how we correct the astrometry in each tile and our iterative technique to remove glitches. Section 3.3 describes the final map products, our method to remove contaminating emission from Galactic cirrus and filtering applied to optimize detection of point sources. Finally, in Section 3.4 we describe the calibration and the differences from the calibration used for the GAMA fields.

3.1. *The SPIRE Bolometer Data*

The SPIRE instrument consists of three imaging arrays for observations at 250, 350, and 500μm with 139, 88, and 43 bolometers, respectively. Each array has two associated thermistors to monitor the temperature of the array, although after launch only one of the 350μm thermistors worked, and two dark bolometers, bolometers that receive no light. In *Herschel* parlance, the 'level-0' data are the raw instrumental/telescope data and the 'level-1' data consist of the calibrated flux-density versus time measurements for the individual bolometers (calibrated timelines), which can then be used to create an image of the sky. In this section we explain the way we produced the calibrated level-1 data.

We converted the level-0 data to the level-1 data, the calibrated timelines, using the *Herschel* Interactive Processing Environment (HIPE, Ott 2010), version 11.0 1200 (development build). Unless described otherwise, we used the standard components of the data-reduction

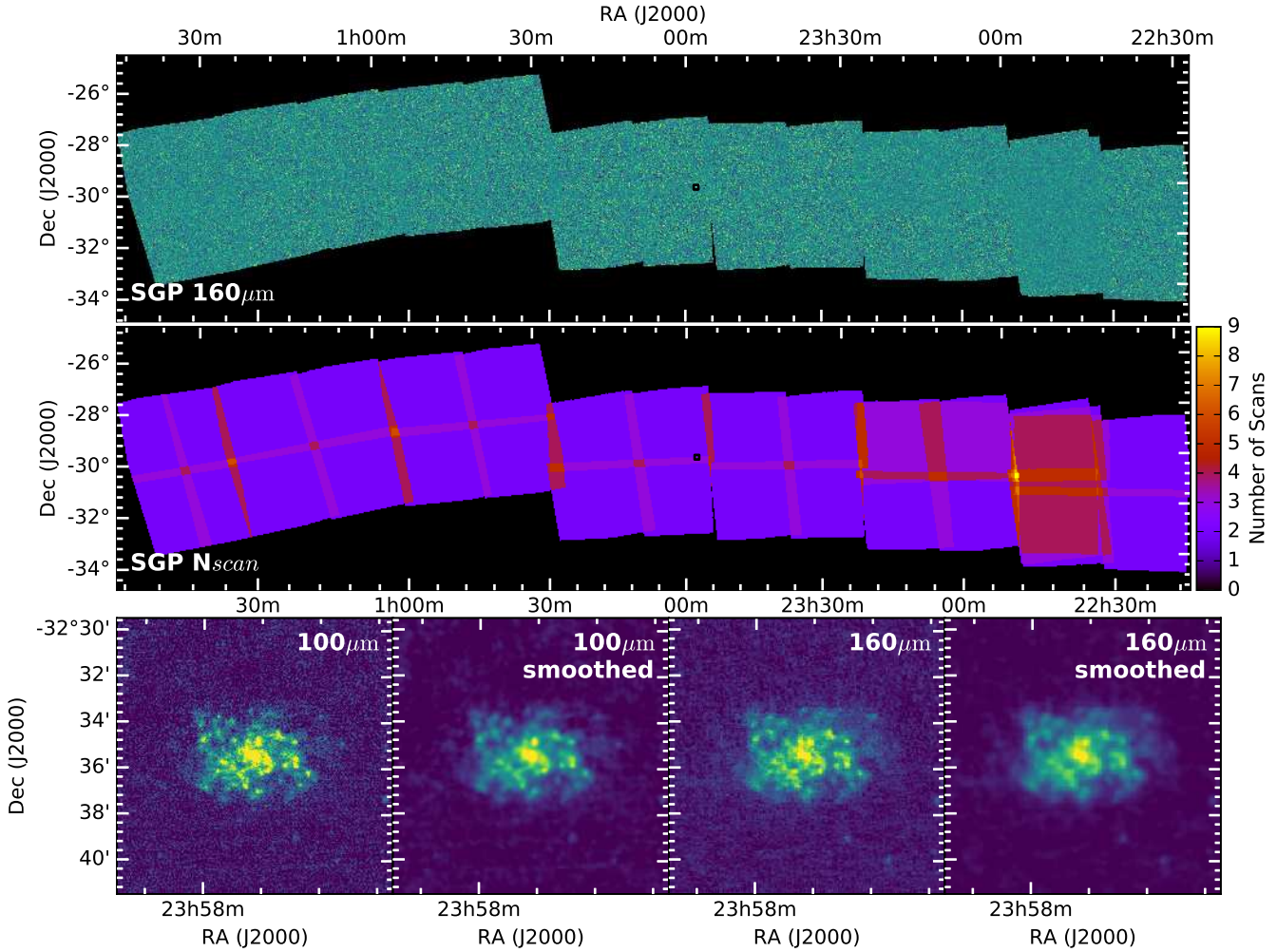

Figure 5. PACS maps of the SGP field. The larger top panels show the 160μm map *(top)* and the number of observations (N_{scan}) from which the map was made *(middle)*. Note the difference from the coverage maps shown in Figures 4; there are several regions where there are extra data for PACS because of parallel-mode observations performed to replace failed SPIRE observations, and there is also the area at the western edge of the field where we were unable to get a replacement for a failed SPIRE observation (Figure 4) but the PACS observation was fine. The row of lower panels show close-up images of the area around the nearby galaxy NGC 7793, which is shown by the black rectangle on the top panels, at both PACS wavelengths, both the raw images and images smoothed by a Gaussian with the same full-width at half maximum as the point-spread function.

pipeline. Forty two of 51 observations for the NGP and SGP fell in observing days 320–761, during which there were positional offsets caused by a change in the operating temperature of the star-tracker camera for which the camera was not re-calibrated. We used an updated pointing model released by the *Herschel Science Centre* in 2012 to correct the pointing for these observations.

We corrected glitches in the bolometer and thermistor data using a different technique from the standard module in the pipeline. Instead of the default wavelet deglitcher, we used the sigma-kappa deglitcher, since tests on both our *H*-ATLAS data and on data from the *Herschel* Virgo Infrared Cluster Survey (HeViCS, Davies et al. 2010) showed it performed better for parallel-mode observations with high scan-speeds and a reduced (10 Hz) sampling rate (the non-default settings for the SIGMAKAPPADEGLITCHER task were: kappa=3.5, gamma=0.1, boxFilterCascade=5, largeGlitchRemovalTimeConstant=7, iterationNumber=3).

At this point, we had calibrated timeline data (level-1) but the data were still affected by artefacts, including 'jumps' and gradual changes in the signal caused by changes in the temperature of the bolometers. The thermistor timeline data contained the necessary information to correct for the effect of temperature. Since the 350μm array only had one working thermistor, we used dark-bolometer 1 as a replacement. However, before we corrected the bolometer timelines, it was necessary to correct both the bolometer and thermistor timelines for the jumps.

A jump is an instantaneous change in the voltage of an individual bolometer or thermistor (a typical example is shown in Figure 6). In rare cases, rather than a step change in voltage, there is a sudden large change followed by a gradual decay back toward the original value. Jumps appear to be more common in thermistors than bolometers. Our jump correction method (see below) does not work well in correcting these rare jumps, and if one of these occurred in a thermistor, we used one of the dark bolometers as a replacement when correcting the bolometer timelines for the effect of temperature. We looked for jumps in bolometers and thermistors in different ways.

For the thermistors, rather than using the automatic jump detector, we inspected both thermistor timelines for each array by eye to spot jumps in the timelines, using the Kst visualization tool[1] In the case of the 350μm array, we carried out a similar inspection of the timelines of dark-bolometer 1.

It was not practical to search for jumps in the bolometer timelines in the same way because there were too many of them. Instead we made initial maps of each individual observation from the timelines and visually searched for the light and dark thin streaks caused by jumps; since a single H-ATLAS observation consists of scans in a single direction and one map pixel usually only includes data from a few bolometers, the effects of a jump are easy to see.

Before correcting the jumps, we combined all scan legs from an observation, including the "turn-around" data, into a single timeline. We then corrected all the jumps in the timeline by fitting a linear relationship to portions of the timeline immediately before and after the jump, and then adding the difference in these relationships to the timeline after the jump (see Smith 2012, for more details). We replaced the samples immediately around the jump (Figure 6) with random noise, and these samples were then masked and not used to make the final maps.

The advantage of combining the data from all scan legs into a single timeline is that makes it possible to remove more accurately the drift in the bolometer signals caused by temperature changes. In the standard pipeline, this correction is done separately for each scan leg and the information in the "turn-around" data is not used at all. Before we made the correction for the effect of temperature, we masked any samples in the timelines that had been flagged as bad (e.g., samples effected by glitches, samples in which the signal is saturated) and any places in the timelines where there were obvious bright sources.

[1] Kst is a data visualization tool. For more information see http://kst-plot.kde.org/.

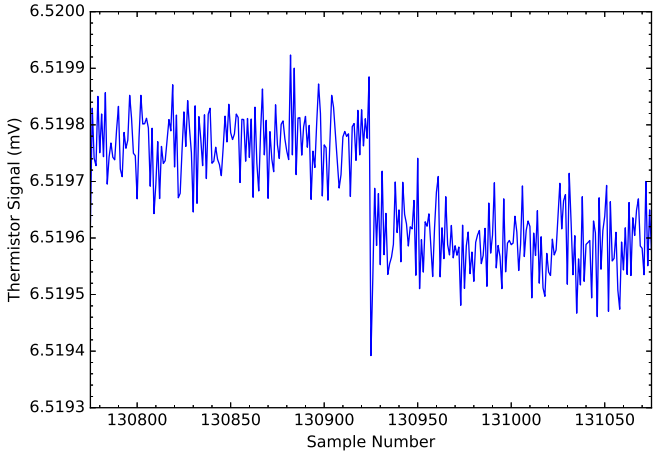

Figure 6. Example of a thermistor 'jump' from one of the thermistors for the 500μm array, PLWT2, during ATLAS observation 1342196626.

We fitted the following relationship between the signal measured by a single thermistor (S_T) and the signal measured by the ith bolometer ($S_{\mathrm{bolom},i}$): $S_{\mathrm{bolom},i} = a \times S_T + c$. We then subtracted this relationship from the bolometer signal, effectively removing the effect of the temperature change. A difference from our procedure in the GAMA fields (V16) is that we carried out this fit for both thermistors, and then used the thermistor that produced the best fit to the data to correct the bolometer timelines. For the 350μm timelines, we did the fits for the one working thermistor and for dark-bolometer 1. For any observation for which one of the thermistors was saturated or affected by a jump that could not be accurately corrected (see above), we used one of the dark bolometers rather than the thermistor. There were parts of some timelines where the linear relationship given above did not provide a good fit to the data. These almost always occurred six hours after a cycle of the SPIRE cooling system and became known as "cooler burps". In cooler burp regions the timelines vary far more more rapidly than the average SPIRE timeline. For these timelines we fitted a fifth-order polynomial rather than a linear relationship.

Once the thermal drift correction had been applied, we applied a high-pass filter to remove any residual drifts. Before applying the filter, we removed the brightest sources from the timelines, and then restored these after the filtering. The high-pass filter corresponds to a scale on the sky of 4.2°, which was chosen to minimize the $1/f$ noise on the images (Pascale et al. 2011). Our images will therefore not contain any structures on scales larger than this. In practice, however, one of the effects

of our scanning method is that any structure on scales >20′ is attenuated (Waskett et al. 2007, see Section 5.4 for more details).

3.2. *Initial Maps and Astrometry*

The next step in the data reduction was to make maps from each individual observation. The two purposes of these initial maps were to check the astrometry of each observation and to remove more bad data, since some low-level artefacts and samples containing bad data are easier to find on the maps than in the timelines.

We carried out our astrometric calibration of the observations in the NGP using the technique that is described more fully in Smith et al. (2011). Briefly, we produced initial source catalogs for each map using our source-detection method (V16). We then produced histograms of the differences in RA and Dec between the positions of the sources and the positions of all objects on the SDSS DR7 r-band images (Abazajian et al. 2009) within 50″ of each source. We then fitted these distributions using a Gaussian model for the SPIRE positional errors, allowing for the effect of clustering in the SDSS data (see Smith et al. 2011, for the details). This procedure allowed us to measure the average difference in positions in both R.A. and decl. for each dataset between the *Herschel* positions and the SDSS positions with a precision of ∼0.05 arcsec in each direction. The shifts we found ranged from less than an arcsec to a few arcsec, in agreement with the 1σ pointing uncertainty of ∼2 arcsec given for *Herschel* (Pilbratt et al. 2010). We used these shifts to correct the astromometry for each *Herschel* observation, so that the effective calibration of the NGP maps and catalogs should be the same as the SDSS.

The SGP field is not covered by the SDSS. To calibrate the astrometry of the SGP observations, we used the same method as above but we replaced the SDSS catalogue with the catalogue from the VLT Survey Telescope ATLAS (Shanks et al. 2015). We found astrometric shifts of a similar size to those for the NGP except a few tiles with corrections of ∼4 arcsec.

We also used these initial single-observation maps to look for any residual artefacts. In particular, the standard deglitcher modules (Section 3.1) do not completely mask very large glitches, due to a parameter which limits the maximum number of samples that can be masked. These unmasked samples produce 'glitch tails' on the images, linear features in the scan direction. We looked for these by eye on the map and then masked the appropriate parts of the timelines.

We also used a new iterative technique to look for glitches that were too faint to be detected by algorithms that work on the timelines. This technique was not applied to the data for the GAMA fields, since we developed it after our first data release. In this technique, we look for bolometer samples that are discrepant by at least 5σ from the value predicted from the statistics of the map. The first step in the procedure is to use all the observations to make a low-resolution map of each field with three times the default pixel size (Section 3.3). The flux in each pixel, $F_{\rm MapPixel}$, is the mean of the fluxes of the $N_{\rm Pixel}$ timeline samples that fall within that pixel. If $F_{\rm Sample}$ is the flux density of a single bolometer sample and $\sigma_{\rm MapPixel}$ is the error in $F_{\rm MapPixel}$, we treat a sample as bad, and thus mask it, if

$$\frac{F_{\rm Sample} - F_{\rm MapPixel}}{\sigma_{\rm MapPixel}\sqrt{N_{\rm Pixel}}} > 5 \qquad (1)$$

After masking all the discrepant samples in the timelines, we remade the maps and looked for additional samples that met the criterion in equation 1. We carried out four iterations of this procedure, masking in total 295,496 and 539,126 bolometer samples for the NGP and SGP, respectively, which equates to ∼0.02% of all bolometer samples.

As the final step in the processing of the timelines, we masked the "turn around" data (i.e., regions where the satellite was not scanning at a constant speed) at the end of each scan leg.

3.3. *The Final SPIRE Maps*

We created the final maps by combining all the corrected and masked level-1 data for each field. We used the simple ('naive') map-maker in which the flux density in each pixel is taken to be the mean flux density of all the bolometer samples that contribute to that pixel. Despite the concern before launch (Section 2; Waskett et al. 2007) that sophisticated map-making algorithms would be necessary to remove large-scale artefacts, the use of the thermistors to correct for the thermal drift of the arrays worked well enough that this simplest of all map-making techniques was sufficient. As for the GAMA fields (V16), we used a pixel size of 6″, 8″, 12″ for the 250, 350, and 500μm bands, respectively, which are different from the default pixel sizes of *Herschel* images; we chose them because they correspond to roughly one third of the size of the PSF (full-width half maximum; FWHM) in each band (see below) and they are big enough that the chance of a map pixel containing no bolometer samples, thus producing a Not-a-Number (NaN) pixel, is low. The 250μm maps for both fields are shown in Figures 2 and 4.

The standard pipeline produces an estimate of the uncertainty in the flux density measured in each pixel by

calculating the variance of all the timeline samples that contribute to that pixel. However, this method does not produce an accurate estimate of the flux uncertainty for two reasons: (a) the small number of samples in each pixel means that the error on the uncertainty estimate is quite large; (b) the variance will be too high if the pixel coincides with a bright object. Instead we have produced our own uncertainty maps, using $\sigma_{\rm inst}/\sqrt{N_{\rm sample}}$ as our estimate of the uncertainty in flux density, in which $\sigma_{\rm inst}$ is the instrumental noise for one timeline sample, calculated using the method described in Section 5.1, and $N_{\rm sample}$ is the number of timeline samples contributing to that pixel. This, of course, is an estimate of the uncertainty in flux density arising from instrumental noise and does not include the effect of source confusion (Section 5.2).

For our PSF, we use the same PSF that was determined by V16 from images of Neptune with the same pixel size as the *H*-ATLAS images (see that paper for more details). The FWHM of the azimuthally averaged PSF is 17.8, 24.0, and 35.2 arcsec at 250, 350, and 500μm, respectively.

As part of the data release, we have also produced images optimized for the detection of point sources. The first step in producing these images was to remove any large-scale structure from the images, which is mostly emission from Galactic dust ('cirrus' emission). We removed the cirrus emission using the NEBULISER[2] algorithm developed by the Cambridge Astronomical Survey Unit and we refer the interested reader to V16 for the details of how we did this. The result of the application of NEBULIZER is that the images should not contain any emission, whether from Galactic dust or from outside the Galaxy, with an angular scale $\succeq$3 arcmin.

For an image containing only one point source and instrumental noise, the maximum signal-to-noise for the source is obtained by convolving the image with the PSF (North 1943). However, the noise in the *H*-ATLAS images is a combination of instrumental noise and "confusion noise", the result of the large number of submillimeter sources that are too faint to detect individually but which merge together to form an undulating background to the images. Chapin et al. (2011) have shown how to calculate a convolving function or 'matched filter' that will produce the maximum signal-to-noise for an unresolved source for any ratio of confusion to instrumental noise. As part of this data release, we have produced images optimized for finding point sources by convolving the raw images with the matched filters we used for the GAMA fields (V16). The instrumental noise and confusion noise for the SGP and NGP are actually slightly different than for the GAMA fields (see Section 5.1 and 5.2), which means that the matched filters we have used are not precisely optimized, but this small disadvantage is outweighed by our being able to use the results of the extensive simulations we carried out with the GAMA matched filters (V16). We tested the effect of using a matched filter optimized with our updated noise values and found that the difference in the number and fluxes of sources is negligible. For readers interested in measuring the flux density of a point source, the matched-filtered images are the ones to use.

3.4. *The SPIRE Flux Calibration*

The flux calibration we applied to the images was publicly released as calTree v11. There is no difference between this and the most recent (at the time of writing) flux calibration (calTree v14). Because of the change in the SPIRE calibration, the flux densities for the NGP and SGP are not quite on the same scale as those in the GAMA fields (V16). To create the maps described by V16, we used the SPIRE v5 calibration tree to create the level-1 data, but applied a 1.0067 correction factor to the 350μm data to make the effective calibration the same as calTree v8. Between v8 and v14 the average (multiplicative) change in flux density is 1.0253±0.0012, 1.0182±0.0045, and 1.0125±0.0006 at 250, 350, and 500 μm, respectively. Therefore, to put the *H*-ATLAS GAMA flux densities on the same scale as those for the NGP and SGP, we need to multiply the flux densities from the DR1 release by these factors. Note, however, that because each bolometer is calibrated individually, the actual correction factor for an individual source depends on which individual bolometers crossed that position.

4. THE PACS OBSERVATIONS

We observed the sky simultaneously at 100 and 160μm, using the PACS camera (Poglitsch et al. 2010). While PACS also has a photometric band at 70μm, it cannot observe in both the 70 and 100μm bands at the same time, and we chose to observe in the 100μm band. The passband filters are relatively broad with $\triangle\lambda/\lambda \sim 1/3$ for both wavelengths; the detailed filter response curves can be found in the HIPE calibration product and are shown in the PACS Observer's Manual[3]. Due to the offset between the SPIRE and PACS

[2] http://casu.ast.cam.ac.uk/surveys-projects/software-release/background-filtering

[3] http://herschel.esac.esa.int/Docs/PACS/pdf/pacs_om.pdf

instruments in the focal plane of the telescope, there is a ≃22 arcmin offset in the final PACS and SPIRE images.

The PACS datasets were more challenging to reduce than the SPIRE dataset because they were larger in volume and because the noise power on the PACS images has a weak dependence on spatial frequency ($\propto 1/f^{\alpha}$ with $\alpha \simeq 0.5$), which makes it impossible to reduce the noise by spatial filtering without affecting the properties of extended sources. The PACS datasets for the NGP and SGP were even larger than for the GAMA fields, because each tile is constructed from at least four observations (Figures 3 and 5) rather than the two used to make the GAMA tiles.

We processed the PACS data up to the stage of the calibrated timelines (level-1 data) in exactly the same way as described by V16 for the GAMA fields and we refer the reader to that paper for the details.

We calibrated the astrometry of each observation using a different method from the one we used for the GAMA fields. For the latter we measured the positions on the PACS images of sources also detected on the SPIRE images, and thus tied the PACS astrometry to the SPIRE astrometry and ultimately to the SDSS astrometry. For the SGP and NGP fields we used a different approach. We first made a 'naive' map from each individual observation, in which the flux density in each pixel is estimated from the average of the timeline samples falling in that pixel. We then found all the 3.4μm sources from the *WISE* survey (Wright et al. 2010) that fell within the area covered by the map. Next we extracted small parts of the PACS image centered on each *WISE* source and added these 'cutouts' together to produce an average PACS source. Finally, we measured the offset between the peak of the PACS emission and the expected position from the *WISE* astrometry. We found offsets between 0.2 and 2.0 arcsec. Before making the final maps, we corrected the astrometry of each individual observation using these offsets.

The effect of '$1/f$' noise (see above) is that naive maps made from the PACS data are dominated by noise on large angular scales unless strong filtering is applied. For the GAMA fields, we tested a number of more sophisticated map-making techniques, eventually choosing the *Jscanamorphos* algorithm (Graciá-Carpio et al. 2015), a version installed as part of HIPE of the *Scanamorphos* algorithm (Roussel 2013). We decided to use this algorithm for the SGP and NGP, but then encountered the complication that *Jscanamorphos* could only make a map from two orthogonal observations. If more than two observations are needed, a map is made for each pair and then all maps are averaged together. We adapted the standard HIPE script for *Jscanamorphos* (from developers build 13.0.5130) so that it would allow us to use all four observations simultaneously[4], a necessary requirement to make one of the NGP and SGP tiles due to the scanning strategy. We found no detrimental effects on the PACS images from combining our individual observations with slightly different scan angles or from combining data taken on different observing days. Despite modifying the script to use as little memory as possible and running on a 158 GB RAM machine, the 100μm data of the westernmost field of the SGP with seven observations (instead of the usual four, see Figure 5) could not be processed in one *Jscanamorphos* process. In this one field, we separated the observations into two (each had a coverage of at least two observations), and made tile maps out of each set of data.

We removed residual large-scale $1/f$ noise from the *Jscanamorphos* map of each tile by applying NEBULISER. This applies an iterative sliding median and linear filter to remove large-scale structure in an image. We set the filter to remove emission on scales above 300″ for both the 100 and 160μm bands. We chose this value to preserve the flux from galaxies smaller than ≃100″ in radius, which is true of all but a few of the biggest galaxies in the fields (for these the flux densities can be measured from the raw *Jscanamorphos* maps). After the application of NEBULISER, we cropped each map to an area covered by at least two orthogonal observations, which ensured that the final images should have no large-scale artefacts caused by the $1/f$ PACS noise.

We applied SWarp[5] (v2.19.1, Bertin et al. 2002) to mosaic the individual tiles and create the final maps for this data release. These images have a pixel size of 3 and 4″ at 100 and 160μm band, respectively, which is roughly one third of the size of the PACS PSF (FWHM). We have also provided, as part of the data release, images showing the number of observations (N_{scan}) contributing to the flux density in each pixel. Figures 3 and 5 show the PACS 160μm images and the N_{scan} images for both fields. The lack of any regions with $N_{scan} = 1$ is because of the requirement that there be at least two roughly orthogonal scans contributing to each pixel.

The PACS PSF depends on the observing mode, the pixel size in the map, the spectral energy distribution (SED) of the source, and the algorithm used to make the map (Lutz 2015). A particular problem is that in parallel mode with fast-scanning (60″/s) the PSF is elongated in the scan direction, especially at 100μm, because of the on-board averaging of the PACS data necessary to trans-

[4] The script is available on GitHub https://github.com/mwls/Public-Scripts.

[5] http://astromatic.iap.fr/software/swarp

mit both the PACS and SPIRE data to Earth. For the GAMA fields we developed a method of constructing an empirical PSF from the data themselves (V16). It was not possible to use this method on the NGP and SGP fields because they were not covered by the GAMA survey, so we have simply assumed our analysis of the PSF in the GAMA fields can be used for the NGP and SGP, as observing mode, pixel sizes, and mapping algorithm are almost identical.

We fitted an azimuthally symmetric Gaussian to the empirical PSF, obtaining a value for the FWHM of 11.4 and 13.7 arcsec at 100 and 160μm, respectively. Exact PSFs could be calculated (e.g., Bocchio et al. 2016) based on the scanning angle of the observations, but due to the large number of combinations of observations, we considered this impractical. We recommend that anyone wishing to convolve the images should use these Gaussians rather than the empirical PSF, which we have not released because our method for constructing the empirical PSF leads to some systematic uncertainty in the values of the central pixels.

For those interested in aperture photometry, we have provided as part of the data release a table listing the encircled energy fraction (EEF) of the PSF against radius. This is derived from our empirical PSF for radii less than 30 arcsec and from the EEF produced by the PACS team for radii between 30 and 1000 arcsec; we refer the reader to V16 for how this was done.

5. PHOTOMETRY ON THE SPIRE IMAGES

In this section we describe an investigation of the characteristics of the SPIRE images and give the reader the information necessary to carry out photometry on the images, both of point sources and extended sources. We first describe an investigation of the instrumental noise and the confusion noise, which both make a significant contribution to the total noise on the images.

5.1. *The SPIRE Instrumental Noise*

In determining the instrumental noise, the first step is to remove any real astronomical signal (e.g. galaxies, cirrus, confusion noise) by creating a jackknife map from subtracting two images of the same part of the sky made from individual SPIRE observations. The instrumental noise can then be measured from the jackknife map. For all pixels in both the NGP and SGP that are covered by at least two individual observations, we calculated the instrumental noise per single bolometer sample from:

$$\sigma_{\rm Sample} = \sqrt{\frac{\sum_{i}^{\rm Npix} (M_{{\rm ortho},i} - M_{{\rm nom},i})^2}{\sum_{i}^{\rm Npix} \left(\frac{1}{C_{{\rm ortho},i}} + \frac{1}{C_{{\rm nom},i}}\right)}} \qquad (2)$$

in which $M_{{\rm ortho},i}$ and $M_{{\rm nom},i}$ are the flux densities in the ith pixel in the two maps out of which the jackknife is made (the flux in the jackknife map is $M_{{\rm ortho},i} - M_{{\rm nom},i}$) and $C_{{\rm ortho},i}$ and $C_{{\rm nom},i}$ are the numbers of timeline samples contributing to the ith pixel in the two maps. We measured the uncertainty on $\sigma_{\rm Sample}$ by randomly assigning the pixels to four groups and calculating $\sigma_{\rm Sample}$ separately for each group. We repeated this five times, which was enough to give a reasonable estimate of the uncertainty in $\sigma_{\rm Sample}$.

We measured the noise per bolometer sample separately for the SGP and NGP fields and the values are given in Table 1. There is generally good agreement between the two fields: a difference of $\simeq$0.1 mJy at 250 and 350μm and $\simeq$0.6 mJy at 500μm. These differences are much greater than the measured uncertainty; we do not know the reason for this but it does not seem likely to have any practical consequences. The averages of the noise values for the two fields are 31.38, 32.08, and 36.21 mJy beam^{-1} at 250, 350, and 500μm, respectively. After adjusting for the small difference in average calibration (Section 3.4), these values are higher at 250 and 350μm than those reported in V16 for the GAMA fields and lower at 500μm, but the difference is for all bands is $<$2%.

A common assumption is that the instrumental noise in *Herschel* images is Gaussian. We have tested this in Figure 7. We have divided the pixels in the jackknife maps by the number of timeline samples each contains, only keeping pixels that have the same number of samples in both of the maps used to make the jackknife. The figure shows the noise per pixel plotted against the number of timeline samples contributing to the pixel (C_i). If the noise is Gaussian, we would expect the noise per pixel to decrease as $C_i^{-1/2}$. The dashed lines in the figure show the predictions of this Gaussian model, using our noise-per-sample estimates. The model agrees almost exactly with the observations, confirming that the instrumental noise does have Gaussian statistical properties.

As part of the data release, we have produced maps showing the noise per pixel in the two fields. As our estimate of the instrumental noise in each pixel, we have used $\sigma_{\rm Sample}/\sqrt{C_i}$, in which $\sigma_{\rm Sample}$ is given in the top panel of Table 1 and C_i is the number of timeline samples in each pixel. As a useful guide to the instrumental noise in parts of the raw and matched-filtered images made with different numbers of scans, in Table 1 (bottom panel) we have given the average instrumental noise for map pixels produced from data from $N_{\rm scan}$ individual observations, with values of $N_{\rm scan}$ from 1 to 7.

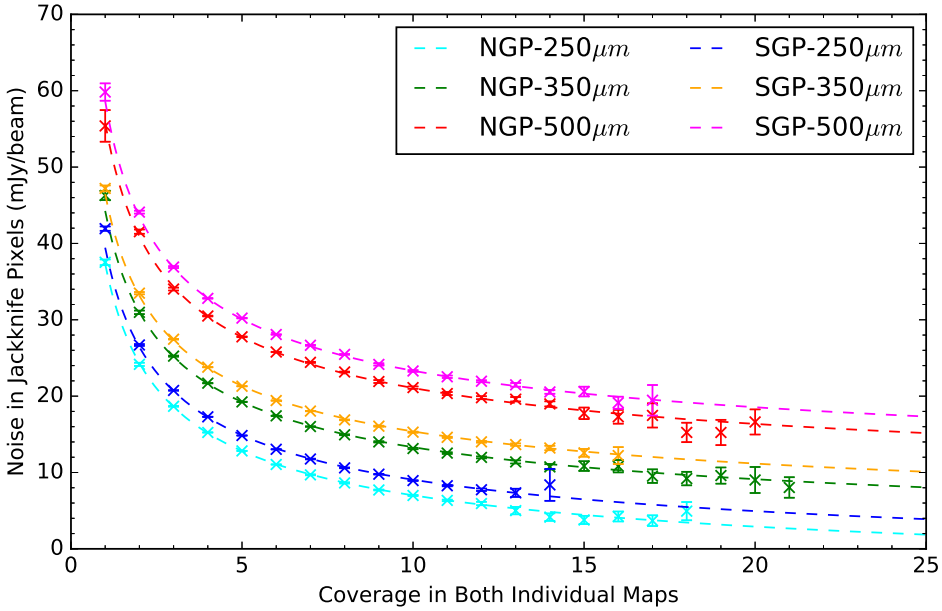

Figure 7. Data points show the standard deviation of the pixels in the jackknife map plotted against the number of timeline samples (C_i) in each pixel; we have only included pixels in which there were the same number of timeline samples in both maps used to make the jackknife. We only plotted values of C_i for which there were at least 30 pixels in the jackknife map. To ensure the data points do not overlap, an offset of -7, -5, -1, +1, +5, +7 mJy beam^{-1} has been applied to the results for NGP-250μm, SGP-250μm, NGP-350μm, SGP-350μm, NGP-500μm, SGP-500μm, respectively. The dashed lines show the predicted noise from our noise-per-sample measurements assuming Gaussian noise.

5.2. *The SPIRE Confusion Noise*

By far a more difficult quantity to define and measure is the confusion noise (as V16 says, "confusion is confusing"), and different scientific objectives require different methods for measuring it. Source confusion has several different effects on observations. Two of the most important are: (a) confusion increases the difficulty of detecting sources by increasing the overall noise on an image; (b) confusion increases the error on the flux measurements. V16 used two different definitions of confusion noise: one suitable for measuring the signal-to-noise with which sources are detected on an image and one suitable for estimating the errors in flux measurements. We have used the same two definitions of confusion, but improved the methods for measuring them described in V16.

The first method was designed to produce a confusion estimate suitable for measuring the noise in signal-to-noise estimates. V16 estimated this using the histogram of pixel values in the SPIRE maps (Figure 8). The shape of this distribution is produced by the instrumental and confusion noise in the maps and the significant individual sources, which produce the right-hand tail in the figure. On the assumption that the tail of individual sources is not relevant for estimating the noise in signal-to-noise estimates, V16 measured the confusion noise by first fitting a Gaussian to the negative part of the pixel histogram, thus avoiding the positive tail, and then calculating $\sqrt{\sigma_{\rm tot}^2 - \sigma_{\rm inst}^2}$, in which $\sigma_{\rm tot}$ is the standard deviation of the best-fitting Gaussian and $\sigma_{\rm inst}$ is the standard deviation of the Gaussian distribution for the instrumental noise.

Here we have used the same definition of confusion noise but a slightly different approach for measuring it. We used the coverage map and noise-per-sample measurements to generate an artificial image containing only instrumental noise. We then fit for the confusion noise (using the Python lmfit package) by adding the confusion noise to our artificial map assuming the confusion noise has a Gaussian distribution. A χ^2 statistic is calculated from the difference between the real pixel histogram and that from the model image; the iteration with the lowest χ^2 value gives our best estimate of the confusion level. To avoid the biasing effect of the positive tail produced by the significant sources, we generally only calculated χ^2 for the negative side of the pixel histogram, with the bins to the right of the peak contributing only if the value for the model lay above the real distribution. We repeated this whole process 96 times to produce an estimate of the error on our mea-

Table 1. SPIRE Instrumental Noise

	Field	Raw Maps			Matched-Filtered Maps		
		250μm (mJy beam^{-1})	350μm (mJy beam^{-1})	500μm (mJy beam^{-1})	250μm (mJy beam^{-1})	350μm (mJy beam^{-1})	500μm (mJy beam^{-1})
Noise per	NGP	31.327 ± 0.005	32.001 ± 0.006	35.922 ± 0.012	-	-	-
Sample	SGP	31.426 ± 0.005	32.149 ± 0.006	36.506 ± 0.006	-	-	-
$N_{scan} = 1$	NGP	19.3715 ± 0.0031	19.2201 ± 0.0036	19.9354 ± 0.0066	10.1834 ± 0.0018	10.0136 ± 0.0021	15.8384 ± 0.0060
	SGP	17.9236 ± 0.0030	17.8210 ± 0.0032	19.4017 ± 0.0034	18.2855 ± 0.0029	18.5682 ± 0.0031	35.3218 ± 0.0093
$N_{scan} = 2$	NGP	10.3446 ± 0.0017	10.1512 ± 0.0019	11.1793 ± 0.0037	5.0488 ± 0.0008	4.9319 ± 0.0010	5.6003 ± 0.0021
	SGP	10.7022 ± 0.0018	10.5098 ± 0.0019	11.7208 ± 0.0020	5.2081 ± 0.0008	5.1019 ± 0.0008	5.8404 ± 0.0015
$N_{scan} = 3$	NGP	8.6163 ± 0.0014	8.4736 ± 0.0016	9.3358 ± 0.0031	4.2170 ± 0.0007	4.1447 ± 0.0009	4.7175 ± 0.0018
	SGP	8.9101 ± 0.0015	8.7633 ± 0.0016	9.7512 ± 0.0017	4.3557 ± 0.0007	4.2836 ± 0.0007	4.9041 ± 0.0013
$N_{scan} = 4$	NGP	7.4953 ± 0.0012	7.3730 ± 0.0014	8.1258 ± 0.0027	3.6817 ± 0.0006	3.6268 ± 0.0007	4.1126 ± 0.0016
	SGP	7.7019 ± 0.0013	7.5780 ± 0.0014	8.4179 ± 0.0015	3.7694 ± 0.0006	3.7243 ± 0.0006	4.2594 ± 0.0011
$N_{scan} = 5$	NGP	6.9083 ± 0.0011	6.8135 ± 0.0013	7.5298 ± 0.0025	3.4204 ± 0.0006	3.3723 ± 0.0007	3.8342 ± 0.0015
	SGP	6.9362 ± 0.0012	6.8602 ± 0.0012	7.6284 ± 0.0013	3.3952 ± 0.0005	3.3831 ± 0.0006	3.8603 ± 0.0010
$N_{scan} = 6$	NGP	6.1648 ± 0.0010	6.0691 ± 0.0011	6.6935 ± 0.0022	3.0391 ± 0.0005	2.9969 ± 0.0006	3.4182 ± 0.0013
	SGP	6.4155 ± 0.0011	6.3283 ± 0.0011	7.0319 ± 0.0012	3.1369 ± 0.0005	3.1289 ± 0.0005	3.5077 ± 0.0009
$N_{scan} = 7$	NGP	5.6386 ± 0.0009	5.5154 ± 0.0010	6.0978 ± 0.0020	2.7739 ± 0.0005	2.7573 ± 0.0006	3.2051 ± 0.0012

NOTE—The instrumental noise properties of the SPIRE maps. The top two rows show the instrumental noise per bolometer sample in the two fields. The other rows correspond to the average instrumental noise per map pixel for pixels with the same number of scans (N_{scan}) for the raw (left) and matched-filtered maps (right).

surement of the confusion noise[6]. The biggest advantage of this method over that of V16 is that we are not assuming a single instrumental noise for the whole map.

Figure 8 shows the artificial histograms that produce the best fit to the histograms for the raw 250μm image of the NGP, the 250μm image from which the background has been subtracted using *Nebulizer*, and the 250μm image from which the background has been subtracted and which has then been convolved with the matched filter. The values of the confusion noise that give the best fit to the data for both the SGP and NGP are given in Table 2 for all three wavebands. Our confusion noise values are the most accurate values produced at the SPIRE wavelengths, with both fields agreeing to within 0.1 mJy beam^{-1} for the nebulised and matched-filtered maps in all bands (the exception is SPIRE 250μm where the difference is 0.14 mJy/beam). This is a significant improvement over V16 whose estimates varied by up to 0.9 mJy/beam between fields. Our confusion values tend to be slightly lower than those of V16 on the nebulised images and slightly higher on the matched-filtered images, which is probably due to the improved method we have used in this paper.

Although the confusion estimates for the NGP and SGP agree well, our uncertainty estimates are so small that the differences between the NGP and SGP are formally significant. Although these fields are very large, it is possible that these differences are due to large-scale interstellar cirrus or to large-scale extragalactic structure (Negrello et al. 2017). Part of the explanation may be that the instrumental noise is such a large part of the total noise, especially in the raw maps, that small errors in the estimate of instrumental noise may lead to large errors in the estimate of confusion noise. Another possible problem may be that our assumption that the source population can be divided into a population of faint confusing sources, which produces a Gaussian pixel distribution, and a population of sources which are de-

[6] Each time we used a different value of the noise per sample, generated from the errors in Table 1, to allow for the uncertainty in this measurement.

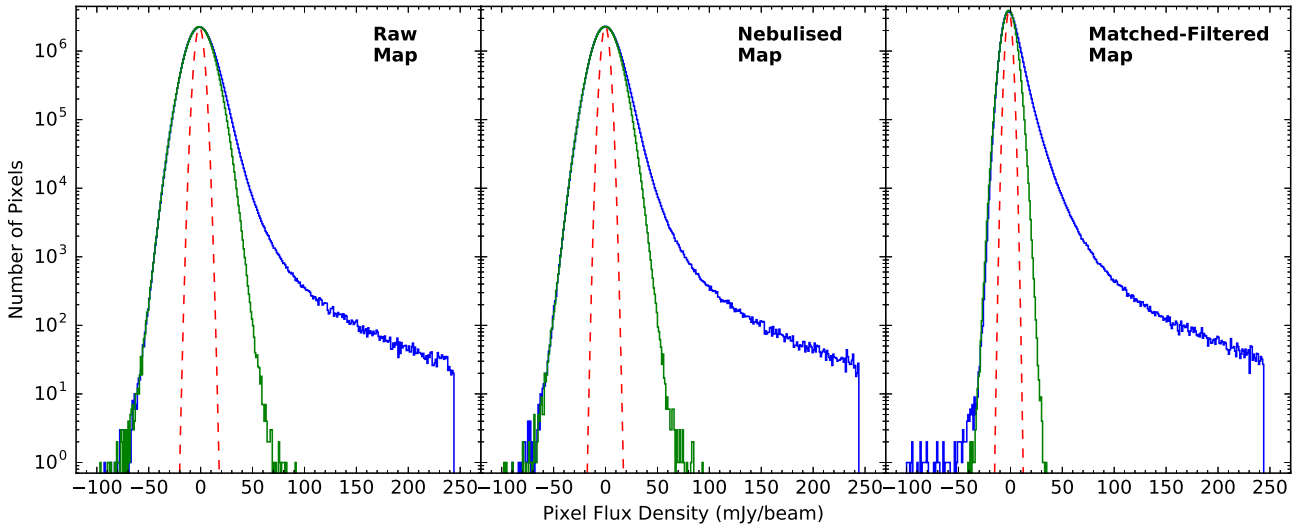

Figure 8. Histogram of pixel flux densities for the raw, nebulised and matched-filtered maps of the NGP at 250μm compared to our model of the noise. The blue lines show the real distribution of pixel fluxes on the map, the green is the histogram from our synthetic noise maps and the red dashed line shows the contribution just from confusion.

Table 2. SPIRE Confusion Noise

	Field	250μm (mJy beam^{-1})	350μm (mJy beam^{-1})	500μm (mJy beam^{-1})
Raw Map	NGP	3.366 ± 0.004	4.517 ± 0.021	4.555 ± 0.011
	SGP	3.516 ± 0.010	4.567 ± 0.031	5.503 ± 0.012
Nebulised	NGP	3.194 ± 0.017	4.129 ± 0.041	4.414 ± 0.018
Map	SGP	3.050 ± 0.015	4.138 ± 0.016	4.495 ± 0.039
Matched-Filter	NGP	2.483 ± 0.017	3.257 ± 0.005	4.436 ± 0.015
Map	SGP	2.470 ± 0.045	3.249 ± 0.005	4.490 ± 0.018

NOTE—The confusion noise estimated by fitting using the histogram fitting method described in Section 5.2.

tected individually and which produce a non-Gaussian tail to the pixel distribution, may be too simplistic.

The second definition of confusion noise used by V16 was one designed to produce an estimate suitable for estimating the errors on flux measurements. Errors on flux measurements are produced by all the other sources on the image, not just the faint ones contributing to the Gaussian distribution in Figure 8 but also the tail of significant sources. The only sources on an image that cannot contribute to the flux error for a source are the pixels in the map that are brighter than that source. To produce an estimate of the confusion noise appropriate for a source with flux density F_s, V16 measured the variance on an image but only included pixels with flux densities $< F_s$. They then took the confusion noise as $\sqrt{\sigma^2_{\rm var} - \sigma^2_{\rm inst}}$, in which $\sigma^2_{\rm var}$ is the variance and $\sigma_{\rm inst}$ is the standard deviation of the Gaussian distribution for the instrumental noise (see V16 for additional details).

The only difference between our method and that of V16 is that we have taken account of the variation in depth over the image arising from different coverage levels, C_i. We have allowed for this by estimating the confusion noise separately for pixels with different numbers of bolometer samples and then averaging the different estimates of the confusion noise.

Figure 9 shows the results for the raw maps and for the maps from which the background has been subtracted using *Nebuliser*. As expected, the confusion noise for the images from which the background (mostly cirrus emission) has not been subtracted is higher than for the

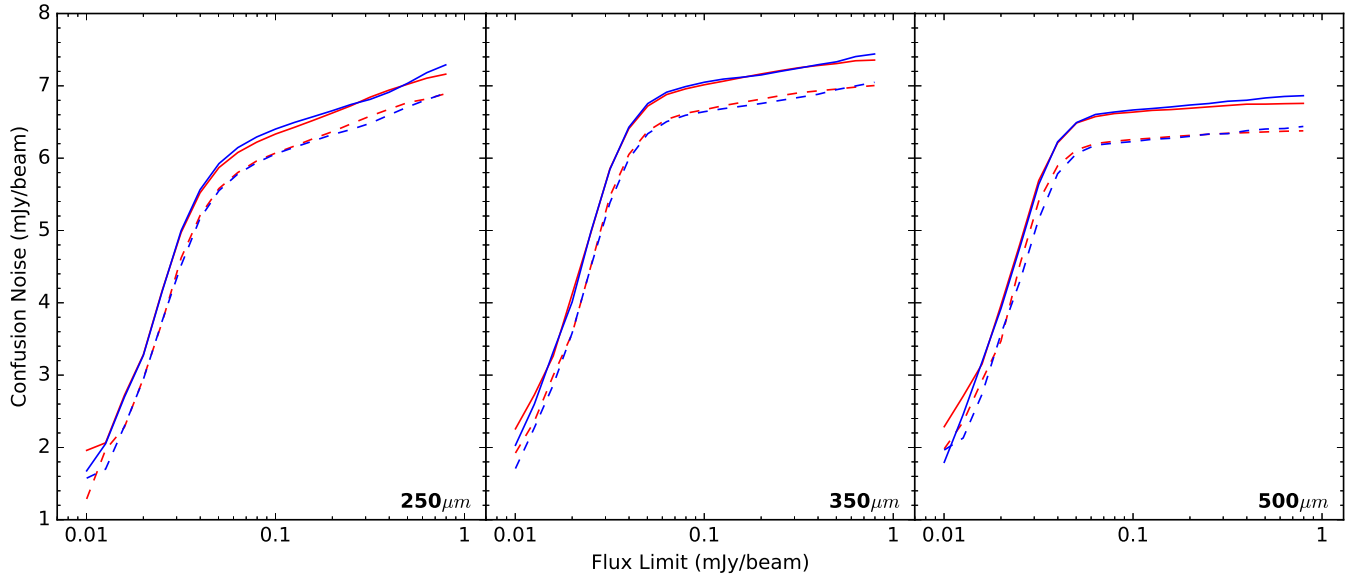

Figure 9. Estimates of confusion noise in the the three SPIRE wavebands using our second method. The red and blue coloured lines represent measurements of the NGP and SGP, respectively. The solid lines are the measurements on the raw-SPIRE maps, while the dashed lines are measurements on the nebulised maps. Uncertainties are not shown as they are too small to plot. The values used to make this plot are given in Table 6 in Appendix B.

images from which the background has been subtracted. The results for the NGP and SGP are almost the same. By definition, the confusion noise depends on F_s. As in V16, we use a value of F_s of 200 mJy to estimate a confusion noise that is easy to compare with the estimates of others. For the background-subtracted maps and with $F_s = 200$ mJy, we find the values of the confusion noise are 6.62, 7.16, 6.69 mJy beam^{-1} at 250, 350, and 500μm, respectively, for the NGP field, and 6.66, 7.15, 6.73 mJy beam^{-1} at 250, 350, and 500μm, respectively, for the SGP field. V16 found mean values of 6.53, 7.03, and 6.58 mJy beam^{-1} for the three GAMA fields at 250, 350, and 500μm, respectively (corrected for the calibration differences), using a very similar method. As for the previous method, the differences between the NGP and the SGP are much smaller than those between the GAMA fields found by V16. Nguyen et al. (2010) estimated the confusion noise in the HERMES survey, using a fairly similar technique to this second method, and derived estimates of 5.8, 6.3, and 6.8 mJy beam^{-1}[7]. The estimates in our work using this technique are broadly similar to those of V16 but systematically higher than those of Nguyen et al. (2010). It is unknown whether these differences are genuinely the result of differences in the source populations in the different fields, or due to the differences in the methods used in the different fields.

By combining our histogram confusion estimates with those of the instrumental noise from Section 5.1, we find the total pixel noise in our nebulised images of 11.0, 11.1, and 12.3 mJy beam^{-1} at 250, 350, and 500μm, respectively. If the matched filter is used to extract point sources is applied to the map, our 1σ map sensitivity estimate is 5.7, 6.0, and 7.3 mJy beam^{-1}, respectively.

5.3. *Photometry for Point and Extended Sources*

The correct method to use for photometry depends on whether the object is expected to be extended or unresolved by the SPIRE PSF. If the object is unresolved, the best method is to use the flux value at the object's position on the SPIRE image that has been convolved with the matched filter. As part of the data release, we have produced a map of the instrumental noise on this image. However, the error on the flux density will also include a component from the confusion noise. The correct value to use for the confusion noise depends on the purpose of the investigation (see the previous section), but for detection experiments we suggest using the values obtained from fitting the Gaussian part of the pixel histograms, which are given in Table 2. For an estimate of the error of the flux density of an individual source, the correct confusion noise value to use would be that obtained from measuring the variance on the image, which depends on the flux density of the source, as shown in Figure 9, and given in Table 6 of Appendix B. Whichever version of the confusion noise is chosen, the confusion

[7] We have not corrected for changes in flux calibration but these changes are much smaller than the differences in the confusion estimates.

noise and the instrumental noise, taken from the map of instrumental noise, should be added in quadrature.

Astronomers interested in carrying out a statistical "stacking analysis", in order to measure the mean sub-millimeter flux density of some class of object, should use the images that have been nebulised to remove cirrus emission. They should be aware that the means of the maps are not necessarily zero and so they should subtract the mean from the map before carrying out the analysis[8]. We recommend using the SIMSTACK algorithm (Viero et al. 2013) or similar, that allows the user to correct for the effects of clustering. We would recommend that astronomers interested in carrying out a stacking analysis should also carry out a Monte Carlo simulation in which they measure the mean flux density at a large number of random positions. This procedure will (a) give an estimate of the mean level on the map and (b) produce an empirical estimate of the error in the stacking measurements.

Photometry of extended sources should be carried out using aperture photometry. The images supplied in the data release have units of Jy beam^{-1}. These can be converted into images with units of Jy pixel^{-1}, suitable for aperture photometry, by dividing the flux value in each pixel by a factor $C_{\rm conv}$, which is given by the area of the telescope's beam divided by the area of a pixel. The current values in the SPIRE Data Reduction Guide[9] are 469.4, 831.2 and 1804.3 arcsec^2 at 250, 350, and 500μm, respectively. Note that it is possible to produce SPIRE maps that have been optimized for aperture photometry, using the SPIRE 'relative gain' method. However, for simplicity, we decided to produce only a single set of maps, optimized for point-source detection.

We recommend carrying out aperture photometry on the images from which the background has been subtracted with *Nebuliser*. The application of *Nebuliser* does mean that the flux density of any sources with a size greater than 3′ might be underestimated,but our tests on the GAMA fields found no evidence of this effect (V16). We also found that the photometric errors were smaller if we used the *nebulised* images. Note that in this case there is no need to subtract the mean map value, since the application of *Nebuliser* should already have subtracted the best estimate of the sky level at that position. Some of the object's emission will fall outside the aperture because of the extended profile of the PSF (Griffin et al. 2013). As part of the data release, we have supplied a table of corrections factors for this effect.

We have carried out Monte Carlo simulations to estimate the errors in the flux densities measured with aperture photometry. We placed apertures randomly on the NGP and SGP maps in areas which are made from two individual observations ($N_{\rm scan} = 2$). The aperture radii were varied in size from approximately the beam size up to 100″, in 2″ intervals, and for each radius we used 3000 random positions. Figure 10 shows the results of the Monte Carlo simulation, and very consistent results between the two fields can be seen.

We assumed the relationship between flux error and radius is a power law, since if the noise is dominated by instrumental random noise we should get a simple linear relationship: flux error $\propto$ radius. We found that we needed to use two power laws to fully describe the relationship at all radii, with the change in relationship occurring at 50″. Our model is described by:

$$\sigma_{\rm ap}({\rm mJy}) = \begin{cases} A r^{\alpha} & \text{if } r \leq 50'' \\ B\,(r-50)^{\beta} + A50^{\alpha} & \text{for } r > 50'' \end{cases} \quad (3)$$

where $\sigma_{\rm ap}$ is the flux error in mJy and r is the radius in arcseconds. The best-fit values for this relationship for all bands and fields are given in Table 3. Above a radius of 50″ the relationship is quite similar to that expected for pure instrumental noise, with values of β between 0.98 and 1.17. Below 50″ the relationship is much steeper with values of α between 1.37 and 1.48. This may be due to small-scale cirrus emission, which would not have been removed with the filtering scale used in *Nebuliser*, or possibly some effect of source confusion.

As the areas where $N_{\rm scan} > 2$ are limited in size, we are unable to perform a Monte Carlo simulation for the deeper regions. As we believe we understand the properties of the instrumental noise, we can account for the differences in $N_{\rm scan}$ by subtracting our instrumental noise for $N_{\rm scan} = 2$ in quadrature and adding back in quadrature the appropriate noise (as measured in Section 5.1, and tabulated in Table 1). The relationship between the flux error and aperture radius, for any value of $N_{\rm scan}$, is then given by:

$$\sigma_{\rm ap}({\rm mJy}) = \begin{cases} \sqrt{(Ar^{\alpha})^2 - X\left(\sigma^2_{\rm inst,2} - \sigma^2_{\rm inst,N}\right) r^2} & \text{if } r \leq 50'' \\ \sqrt{\left(B\,(r-50)^{\beta} + A50^{\alpha}\right)^2 - X\left(\sigma^2_{\rm inst,2} - \sigma^2_{\rm inst,N}\right) r^2} & \text{for } r > 50'' \end{cases}$$

[8] *Nebuliser* produces the best estimate of the sky value at each position but this value is not generally equal to the mean in that region. Therefore, stacking analyses, which sum the emission from large numbers of sources will be sensitive to any small systematic error in the way *Nebuliser* estimates the sky value. To be on the safe side, we therefore recommend that a stacking analysis should only be carried out after the mean has been subtracted from the image.

[9] http://herschel.esac.esa.int/hcss-doc-15.0/index.jsp#spire_drg

(4)

where A, B, α, β are the same as in Equation 3, X is a constant given in Table 3 (which varies between bands) to account for beam area and pixel size, and $\sigma_{\rm inst,N}$ (mJy beam^{-1}) is the instrumental noise for $N_{\rm scan} = N$ as given in Table 1. This equation uses the values of instrumental noise averaged over all the pixels with the same number of scans (Table 1). Purists interested in using the actual instrumental noise at the position of a source can measure this instrumental noise from the noise map, and then obtain the total flux error by modifying equation 4 in a fairly obvious way. If users wish to use elliptical apertures they could either run their own Monte Carlo simulation on the released maps, or a reasonable estimate of the flux error can be obtained by using the estimate for a circular aperture with the same area.

The width of the SPIRE filters mean that both the size of the PSF and the power detected by SPIRE depend on the spectral energy distribution (SED) of the source. The SPIRE data-reduction pipeline is based on the assumption that the flux density of a source depends on frequency^{-1}, and all our images are ultimately based on this assumption. If the user has reason to know the SED of a source, the flux densities should be corrected using the corrections from either Table 5.7 or 5.8 from the SPIRE handbook[10]. It is important to apply these corrections, since they can be quite large: for a point source with a typical dust spectrum (T=20 K, β=2) the multiplicative correction is 0.96, 0.94, and 0.90 at 250, 350, and 500μm, respectively.

Finally, on top of the other flux density errors, there is an error from the uncertainty in the basic flux calibration of the instrument. At the time of writing, the error in the flux density arising from the uncertainty in the absolute flux density of Neptune is 4%, and there is an additional 1.5% error that is uncorrelated between the SPIRE bands (SPIRE Data Reduction Guide). The current recommendation is that these factors should be added linearly, and so the reader should use a calibration error of 5.5%.

5.4. *Power Spectrum of SPIRE Maps*

The primary science goals of *H*-ATLAS are to investigate individual sources, and so our maps were made to optimize the detection and flux-extraction of these small-scale structures. Pascale et al. (2011) used simulations of our observing strategy and map-making techniques to show that there is attenuation of the structure in the *H*-ATLAS maps on scales >20′. Since Pascale et al. (2011) all-sky maps produced by the *Planck* observatory (Planck Collaboration et al. 2011) have been released (Planck Collaboration et al. 2016) which provide a useful 'truth' map to compare with the *H*-ATLAS

[10] http://herschel.esac.esa.int/Docs/SPIRE/spire_handbook.pdf

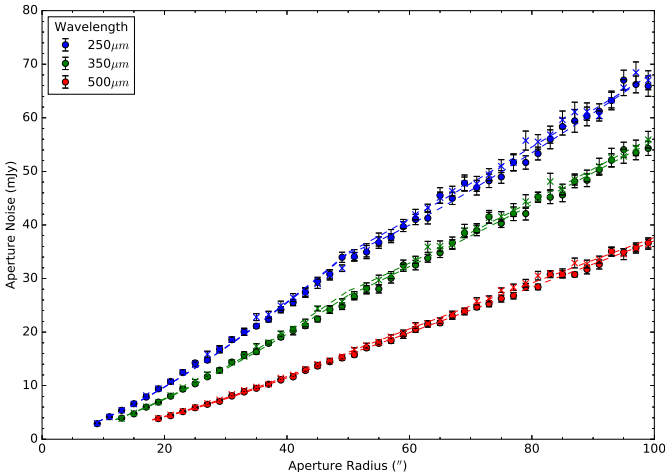

Figure 10. The results of the Monte Carlo simulation of the flux-density errors for aperture photometry on the SPIRE images (see the text for details). The figure shows our estimate of the flux density error plotted against the radius of the aperture. Results from the NGP and SGP are shown by the circular and cross points, respectively. The best-fit power-law models described in Section 5.3 are shown by the dashed lines.

Table 3. Aperture Noise Model Best-fit Parameters

Waveband	Field	A	α	B	β	X
100μm	NGP	0.749	1.475	6.244	0.971	–
	SGP	0.720	1.473	6.235	0.970	
160μm	NGP	0.642	1.444	4.193	0.995	–
	SGP	0.620	1.446	4.247	0.992	
250μm	NGP	0.152	1.388	0.336	1.179	5.13×10^{-4}
	SGP	0.164	1.368	0.527	1.066	
350μm	NGP	0.117	1.389	0.539	1.016	2.91×10^{-4}
	SGP	0.111	1.410	0.497	1.016	
500μm	NGP	0.052	1.464	0.372	1.033	1.39×10^{-4}
	SGP	0.056	1.451	0.459	0.984	

NOTE—The best-fit parameters for the relationship between flux error and aperture radius (Equation 3). See Section 5.3 for details. The X column gives the constant required to correct the relationship for regions of the map with different $N_{\rm scan}$ values (see Equation 4).

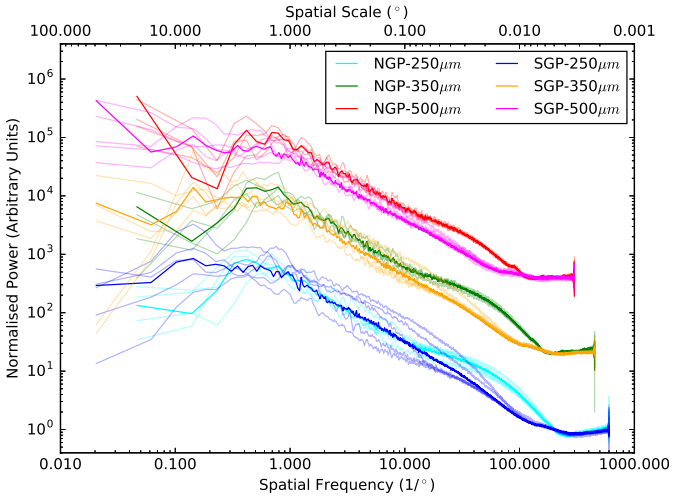

Figure 11. The 1D angular power spectrum of our raw maps for the NGP and SGP fields in the three SPIRE bands. The dark lines show the power spectrum for the entire mosaic, while the lighter lines are for the individual tiles in each mosaic. The profiles in each band are normalized so they have the same value at 0.005°.

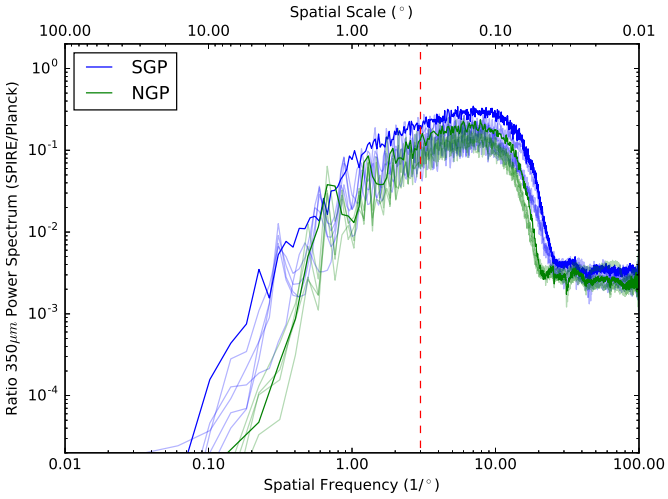

Figure 12. Ratio of the 1D angular power spectra (SPIRE/*Planck*) for the NGP and SGP fields at 350μm. As for Figure 11 the dark lines are for the entire field and the lighter lines are for individual tiles. The red dashed line shows the 20′ scale found by Pascale et al. (2011), where attenuation of emission starts.

maps at 350μm and 500μm. In this section, we calculate the 1D angular power spectrum of our maps (using the agpy package[11]) to investigate what emission scales are preserved in our maps, and if our maps are consistent between tiles.

In Figure 11 we show the 1D power spectrum from the raw SPIRE maps, as well as for each individual tile in the mosaics. The power spectra for each field tend to be in good agreement with each other, especially at 350 and 500μm. The differences between fields is most likely explained due to differences in the cirrus emission. Given the good agreement between tiles in a field, an average 'transfer function' describing the depression of power as a function of angular scale, could be used for each of the two fields.

To test whether the differences seen in Figure 11 are due to variations in the cirrus emission we compare our maps at 350μm with the *Planck* Public Release 2 maps (Planck Collaboration et al. 2016). We first convolved both the NGP and SGP maps to the same resolution as *Planck* using the effective *Planck* beam for our field. Both the *Planck* and SPIRE maps were matched to the same 36″ pixel grid and converted to the same flux-density units. Figure 12 shows the ratio of the 1D power spectra of the SPIRE and *Planck* maps. The ratio maps show broad agreement across all individual tiles and mosaics, confirming that the differences in Figure 11 is due to cirrus emission. At small spatial scales the low ratios of SPIRE/*Planck* power are due to the greater sensitivity of the *H*-ATLAS observations. The low ratios at higher spatial scale are due to the finite size of the maps and the fact that a single SPIRE observation made from scanning the telescope in a single direction will miss large-scale power in the direction orthogonal to the scan direction (Waskett et al. 2007). Our results show the attenuation of emission begins on a scale of ∼15′, broadly in agreement with the value of 20′ found by Pascale et al. (2011). It is possible that our observations affected by 'cooler burps' (see Section 3.1) could have greater attenuation, but, due to the complexity of isolating these regions we did not investigate this further.

In principle, it is possible to correct for this attenuation on large scales using an alternative map-maker (Waskett et al. 2007). If users wish to create maps with alternative map-makers, the authors can be contacted to assist with data/customised timelines. For the 350 and 500μm bands it is also possible to combine the *Herschel* and *Planck* data to create maps that have the correct power on all scales. Of course, the images on large scales will also be affected by cirrus.

6. PHOTOMETRY ON THE PACS MAPS

6.1. *The PACS Instrumental and Confusion Noise*

The PACS maps are very different from the SPIRE maps. The higher instrumental noise means that source confusion is less important and the instrumental noise is correlated between pixels. It is more challenging to measure the confusion and instrumental noise on the

[11] https://github.com/keflavich/agpy/

PACS maps because *Jscanamorphos* uses the existence of multiple PACS observations to remove the effect of temporal changes in the detectors, which means that it is not possible to use jackknifes to estimate the instrumental noise.

To estimate the PACS confusion noise, we used a similar approach to that of Magnelli et al. (2013), who estimated the confusion in the GOODS-S field. We measured the total noise in regions of the map with different number of observations as seen in the N_{scan} maps shown in Figure 3 and 5. To measure the noise, we fitted a Gaussian to the negative part of the histogram of pixel values, using the positive side as an upper limit (similar to what we did for SPIRE in Section 5.2). This gave us a plot of σ_{pix} versus N_{scan}. We then fitted a simple model to this relationship The model has an instrumental noise component, which scales with the number of observations (N_{scan}) contributing to each pixel, and a constant confusion term:

$$\sigma_{pix}(\mathrm{mJy}) = \sqrt{\left(\sigma_{inst}\ N_{scan}^{-0.5}\right)^2 + \sigma_{conf}^2} \quad (5)$$

where σ_{pix} is the total pixel noise in mJy, σ_{inst} is the instrumental noise in mJy for a single PACS observation (N_{scan}=1) , and σ_{conf} is the confusion noise (in mJy). In principle, this procedure allowed us to estimate σ_{inst} and σ_{conf}.

We initially applied this method to our final maps, but found that the noise in the regions in which the tiles overlap is significantly reduced due to the re-projecting procedure used to create the mosaics[12]. We therefore decided to use only the individual tiles, which limited the range of N_{scan} to 2–5, reducing the sensitivity of the method. To regain the sensitivity, we used some observations from the HeViCS survey (Davies et al. 2010), which mapped ∼55 sq. deg. of the Virgo Cluster using the same fast-scan parallel observing mode that we used. While most of the Virgo Cluster was observed in $4^\circ \times 4^\circ$ tiles with eight observations per field, the northernmost Virgo tile was observed 10 times by PACS. We reduced the observations of this tile using the same *Jscanamorphos* method we used for *H*-ATLAS, starting with the level-1 data produced by the standard pipeline. We then made five independent maps from each pair of observations and applied *Nebuliser* to each map, which gave us five maps of the same region of sky. We then averaged various combinations of maps and estimated the total noise on each combined map using the method above, giving us estimates of the total noise from N_{scan} = 2–10. The results of pixel noise versus N_{scan} are shown in Figure 13 for both the *H*-ATLAS and HeViCS results. The values of σ_{inst} and σ_{conf} obtained from fitting Equation 5 to the results for the individual fields are given in Table 4.

[12] In overlapping areas in which N_{scan} = 2 the noise is reduced by a factor of 0.90, 0.91, 0.84 and 0.86 for the NGP 100μm, NGP 160μm, SGP 100μm and SGP 160μm, respectively.

Table 4. PACS Pixel Noise Model Parameters

Waveband	Field	σ_{inst} (mJy)	σ_{conf} (mJy)
100μm	NGP	3.578±0.013	0.393±0.047
	SGP	3.539±0.030	0.603±0.059
	HeViCS	3.774±0.002	0.184±0.004
160μm	NGP	3.515±0.017	0.389±0.055
	SGP	3.532±0.017	0.380±0.058
	HeViCS	3.714±0.001	0.240±0.003

NOTE—The best-fit parameters for the relationship between pixel noise and number of scans (Equation 5). See Section 6.1 for details.

As expected, the estimates of instrumental noise in Table 4 are much higher than the estimates of confusion noise. The errors on the confusion noise estimates for the HeViCS field are much less than those for the NGP and SGP fields because of the larger range of N_{scan}. The confusion noise estimates for the different fields are formally inconsistent, which we suspect arises because the instrumental noise is so much larger than the confusion noise, making any estimate for estimating the confusion noise sensitive to systematic errors (e.g. if the assumption that the noise is Gaussian is slightly wrong). Our most reliable estimates of confusion noise come from the HeViCS tile because of the larger range of N_{scan}, and are 0.184 ± 0.004 and 0.240 ± 0.003 mJy, at 100 and 160μm, respectively. These estimates are broadly similar at 100μm, but differ at 160μm, to those presented by Magnelli et al. (2013) of 0.15 and 0.68 mJy at 100 and 160μm, although these values may not be directly comparable due to differences in pixel size and beam size. Assuming beam areas of 207 and 308 arcsec^2 at 100 and 160μm (calculated from our measured PSFs), the confusion noise is 4.23 and 4.62 mJy beam^{-1} at 100 and 160μm, respectively.

6.2. *Photometry for Point and Extended Sources*

The PACS PSF is not a simple Gaussian and in fast-scan parallel mode is significantly extended in the scan direction (Section 4), which means that it must vary

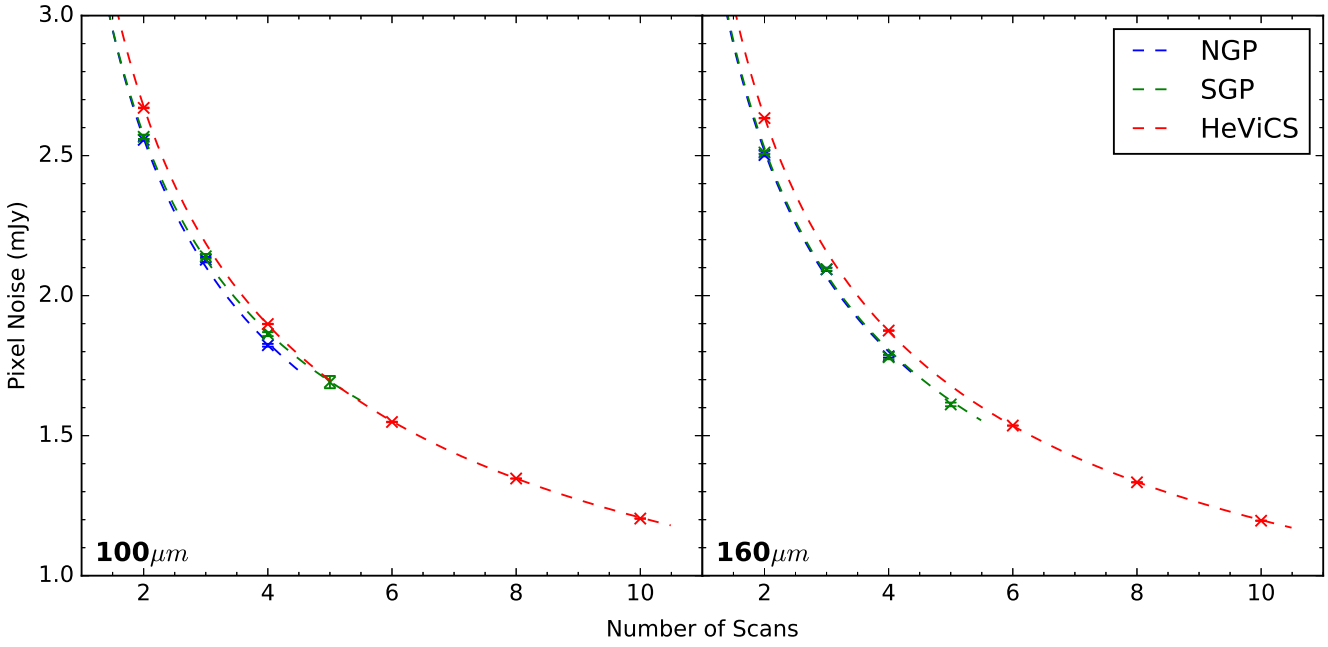

Figure 13. Pixel noise in PACS tiles versus number of observations contributing to each pixel (N_{scan} - see Figure 3 and 5). The blue, green, and red crosses show the measurements from the NGP, SGP and HeViCS fields, respectively. The dashed lines show the best fit of equation 5 to each dataset.

within both fields, especially between points on the maps that are composed of different numbers of individual observations. For this reason, the technique of maximising the signal-to-noise for point sources by convolving the images with the PSF is not as accurate as for the SPIRE images. Instead, we use aperture photometry with a small aperture (see below). However, if the reader does prefer to convolve the map with the PSF, for example for detecting a faint point source, we recommend the use of our Gaussian fit to the empirical PSFs, which have a FWHM of 11.4 and 13.7 arcsec at 100 and 160μm, respectively. Anyone carrying out a stacking analysis should be aware that the means of the PACS maps are not zero, and so the mean of the map should be subtracted before proceeding with the stacking[13]. Errors for a stacking analysis should be obtained from a Monte Carlo analysis in which flux densities are measured at random points in the image.

For photometry of an unresolved source, the alternative to measuring the flux density from an image that has been convolved with the PSF is aperture photometry with an aperture not much larger than the PSF. V16 found that the signal-to-noise peaks for an aperture with a radius of $\simeq$8 arcsec at both wavelengths. We suggest that astronomers wishing to carry out photometry of point sources should use this aperture, although since such a small aperture contains only a small number of pixels, they should think carefully about pixelization effects when using this approach. The units of the PACS maps are Jy pixel^{-1}, so aperture photometry can be carried out by adding up the flux density values for all the pixels within the aperture; there is no need to estimate a sky value because we have already subtracted any residual background emission using *Nebulizer*. As part of the data release, we have supplied a file listing the EEF in the two bands out to a reference radius of 1000 arcsec (see Section 4). Both the flux densities and the flux errors (see below) should be corrected for the fraction of the PSF that is outside the aperture using this table.

Photometry of sources that are expected to be extended, for example nearby galaxies, should also be carried out by aperture photometry. There is no need to estimate a sky value because we have already subtracted any residual background emission using *Nebulizer*. Both the flux densities and the flux errors (see below) should be corrected for the fraction of the PSF that is outside the aperture using the EEF.

We have carried out a similar Monte Carlo simulation to estimate the errors in the flux densities measured in aperture photometry to the one we carried out

[13] As we noted for SPIRE, *Nebuliser* produces an estimate of the sky value at each point but this value is not generally equal to the mean at that point. Therefore, stacking analyses, which sum the emission from large numbers of sources will be sensitive to any small systematic error in the way that *Nebuliser* estimates the background. Therefore, to be safe, the mean should be subtracted from an image before carrying out a stacking analysis.

for SPIRE (Section 5.3). For each aperture radius, we placed 3000 apertures at random positions on the part of each image with $N_{scan} = 2$. We used radii ranging from approximately the size of the beam up to 100 arcsec. The results are shown in Figure 14. As for SPIRE, we fit a power-law relationship (Equation 3) to the results of the Monte-Carlo simulation. The values of the best-fit parameters in this relationship are given in Table 3. As for SPIRE, we found that at large radii the flux error is approximately proportional to the aperture radius, which is the relationship expected for instrumental noise that is not correlated between pixels. At smaller radii, as for SPIRE, we found the flux error increases more rapidly with radius. We are not sure of the explanation but possibilities include cirrus emission that has not been removed because of the large filtering scale used in *Nebuliser* and residual $1/f$ noise not removed by the map-maker. We have not produced maps of the PACS instrumental noise for the data release. Instead, we have produced maps showing the number of individual datasets (N_{scan}) contributing to each pixel. This map and the following equation can then be used to obtain an estimate of the flux density error for any object and any aperture size:

$$\sigma_{ap}(\mathrm{mJy}) = \begin{cases} \sqrt{(Ar^{\alpha})^2 - \frac{\sigma_{inst}^2 \pi}{P^2}\left(\frac{1}{2} - \frac{1}{N_{scan}}\right) r^2} \\ \qquad\qquad \text{if } r \leq 50'' \\ \sqrt{\left(B\,(r-50)^{\beta} + A50^{\alpha}\right)^2 - \frac{\sigma_{inst}^2 \pi}{P^2}\left(\frac{1}{2} - \frac{1}{N_{scan}}\right) r^2} \\ \qquad\qquad \text{for } r > 50'' \end{cases} \quad (6)$$

where A and B are best fit parameters from Table 3, σ_{inst} is the noise in mJy given in Table 4 and P is the pixel size of the maps in arcseconds ($3''$ at 100μm and $4''$ at 160μm). As with SPIRE, if the user wishes to use bespoke elliptical apertures a reasonable estimate can be obtained by using the estimate of the flux uncertainty for a circular aperture with the same area, or alternatively, they could run their own Monte Carlo simulation on the released maps.

On top of the flux density uncertainty given by our power-law model, there is also a fundamental calibration error. As for SPIRE, the dominant uncertainty is due to the models of the calibration objects, in the case of PACS stars and asteroids, which is estimated to be 5% (PACS Calibration page[14]). The reproducibility of calibration sources is measured to be ∼2% (Balog et al. 2014) and so, as in V16, we add the uncertainties and thus make the conservative assumption that the calibration uncertainty is 7%. As with SPIRE, all our measurements of flux density are based on the assumption that flux density is proportional to frequency^{-1}, which introduces an error if the source does not have this SED because of the width of the PACS bandpass filters. We refer anyone wishing to make a correction for this effect to the PACS Color-Correction document[15].

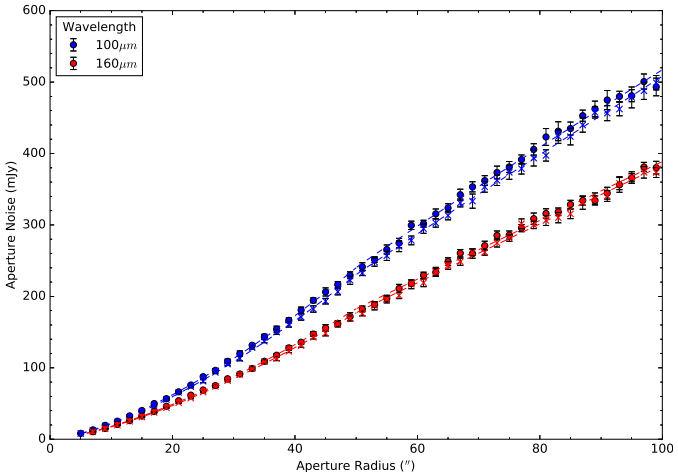

Figure 14. Results of the random Monte Carlo simulation for the two PACS bands, where we place apertures with radius varying from approximately the beam size up to 100″, with 3000 apertures used at each radii. The apertures are only placed on regions with $N_{scan} = 2$. Results from the NGP and SGP are shown by the circular and cross points, respectively. The best fit models described in Section 6.2 are shown by the dashed lines.

7. SUMMARY

We have presented the largest submillimeter images that have been made of the extragalactic sky. The *Herschel* Astrophysical Terahertz Large Area Survey (*H*-ATLAS) is a survey of 660 deg^2 in five photometric bands: 100, 160, 250, 350, and 500μm - with the PACS and SPIRE cameras. We have described the images of a field 180.1 deg^2 in size centered on the north Galactic Pole (NGP) and of a field 317.6 deg^2 in size centred on the south Galactic pole. The NGP field contains the Coma cluster. Over most of the images, the pixel noise, including both instrumental noise and confusion noise, is approximately 3.6, 3.5 mJy at 100, 160μm, and 11.0, 11.1, and 12.3 mJy beam^{-1} at 250, 350, and 500μm, but reaches lower values in some parts of the images. We have described the results of an investigation of the noise properties of the images. We make the most precise estimate of confusion in SPIRE maps to date, finding a value of 3.12 ± 0.07, 4.13 ± 0.02, and

[14] http://herschel.esac.esa.int/twiki/bin/view/Public/PacsCalibrationWeb

[15] http://herschel.esac.esa.int/twiki/pub/Public/PacsCalibrationWeb/cc_report_v1.pdf

4.45 ± 0.04 mJy beam^{-1} at 250, 350, and 500μm in our un-convolved maps. For PACS we find an estimate of confusion in our fast-parallel observations of 0.18 and 0.24 mJy at 100 and 160μm. The values of the confusion noise that we have measured are similar but not identical to the values from other *Herschel* surveys. Finally, we have given recipes for using these images to carry out photometry of objects, both objects expected to be unresolved and those expected to be extended.

M.W.L.S and S.E. acknowledge support from the European Research Council (ERC) Forward Progress 7 (FP7) project HELP. L.D., S.J.M. and H.G. acknowledge support from the ERC Consolidated grant cosmic dust. L.D., S.J.M. and R.J.I. acknowledge support from the ERC Advanced Investigator grant COSMICISM. E.V. and S.A.E. acknowledge funding from the UK Science and Technology Facilities Council consolidated grant ST/K000926/1.

We thank everyone involved with the *Herschel Space Observatory*.

Herschel is an ESA space observatory with science instruments provided by European-led Principal Investigator consortia and with important participation from NASA. The Herschel spacecraft was designed, built, tested, and launched under a contract to ESA managed by the *Herschel/Planck* Project team by an industrial consortium under the overall responsibility of the prime contractor Thales Alenia Space (Cannes), and including Astrium (Friedrichshafen) responsible for the payload module and for system testing at spacecraft level, Thales Alenia Space (Turin) responsible for the service module, and Astrium (Toulouse) responsible for the telescope, with in excess of a hundred subcontractors.

HIPE is a joint development by the *Herschel* Science Ground Segment Consortium, consisting of ESA, the NASA *Herschel* Science Center and the HIFI, PACS, and SPIRE consortia.

Facilities: *Herschel*

Software: numpy (Van Der Walt et al. 2011), scipy (Jones et al. 2001–), Astropy (Astropy Collaboration et al. 2013), APLpy (Robitaille & Bressert 2012), LMFIT, agpy.

REFERENCES

Abazajian, K. N., Adelman-McCarthy, J. K., Agüeros, M. A., et al. 2009, ApJS, 182, 543

Astropy Collaboration, Robitaille, T. P., Tollerud, E. J., et al. 2013, A&A, 558, A33

Balog, Z., Müller, T., Nielbock, M., et al. 2014, Experimental Astronomy, 37, 129

Bertin, E., Mellier, Y., Radovich, M., et al. 2002, in Astronomical Society of the Pacific Conference Series, Vol. 281, Astronomical Data Analysis Software and Systems XI, ed. D. A. Bohlender, D. Durand, & T. H. Handley, 228

Blain, A. W., & Longair, M. S. 1993, MNRAS, 264, 509

Bocchio, M., Bianchi, S., Hunt, L. K., & Schneider, R. 2016, A&A, 586, A8

Bourne, N., Dunne, L., Maddox, S. J., et al. 2016, MNRAS, 462, 1714

Chambers, K. C., Magnier, E. A., Metcalfe, N., et al. 2016, ArXiv e-prints, arXiv:1612.05560

Chapin, E. L., Chapman, S. C., Coppin, K. E., et al. 2011, MNRAS, 411, 505

Colless, M., Dalton, G., Maddox, S., et al. 2001, MNRAS, 328, 1039

Dark Energy Survey Collaboration, Abbott, T., Abdalla, F. B., et al. 2016, MNRAS, 460, 1270

Davies, J. I., Baes, M., Bendo, G. J., et al. 2010, A&A, 518, L48

de Jong, J. T. A., Kuijken, K., Applegate, D., et al. 2013, The Messenger, 154, 44

Driver, S. P., Norberg, P., Baldry, I. K., et al. 2009, Astronomy and Geophysics, 50, 5.12

Dunne, L., Gomez, H. L., da Cunha, E., et al. 2011, MNRAS, 417, 1510

Eales, S., de Vis, P., Smith, M. W. L., et al. 2017, MNRAS, 465, 3125

Eales, S., Dunne, L., Clements, D., et al. 2010, PASP, 122, 499

Edge, A., Sutherland, W., Kuijken, K., et al. 2013, The Messenger, 154, 32

Fernique, P., Boch, T., Donaldson, T., et al. 2014, MOC - HEALPix Multi-Order Coverage map Version 1.0, IVOA Recommendation 02 June 2014, , , arXiv:1505.02937

Fuller, C., Davies, J. I., Smith, M. W. L., et al. 2016, MNRAS, 458, 582

Furlanetto, C., Dye, S., Bourne, N., et al. 2017, MNRAS, Submitted

González-Nuevo, J., Lapi, A., Fleuren, S., et al. 2012, ApJ, 749, 65

Graciá-Carpio, J., Wetzstein, M., & Roussel, H. 2015, ArXiv e-prints, arXiv:1512.03252

Griffin, M. J., Abergel, A., Abreu, A., et al. 2010, A&A, 518, L3
Griffin, M. J., North, C. E., Schulz, B., et al. 2013, MNRAS, 434, 992
Ibar, E., Ivison, R. J., Cava, A., et al. 2010, MNRAS, 409, 38
Ivison, R. J., Lewis, A. J. R., Weiss, A., et al. 2016, ApJ, 832, 78
Jones, E., Oliphant, T., Peterson, P., et al. 2001–, SciPy: Open source scientific tools for Python, , , [Online; accessed <today>]. http://www.scipy.org/
Lapi, A., González-Nuevo, J., Fan, L., et al. 2011, ApJ, 742, 24
Lawrence, A., Warren, S. J., Almaini, O., et al. 2007, MNRAS, 379, 1599
Liske, J., Baldry, I. K., Driver, S. P., et al. 2015, MNRAS, 452, 2087
Lutz, D. 2015, *Herschel Space Observatory*, http://herschel.esac.esa.int/twiki/pub/Public/PacsCalibrationWeb/bolopsf_22.pdf
Maddox, S., Valiante, E., Eales, S., & Smith, M. W. L. 2017, MNRAS, Submitted
Magnelli, B., Popesso, P., Berta, S., et al. 2013, A&A, 553, A132
Negrello, M., Hopwood, R., De Zotti, G., et al. 2010, Science, 330, 800
Negrello, M., Amber, S., Amvrosiadis, A., et al. 2017, MNRAS, 465, 3558
Neugebauer, G., Habing, H. J., van Duinen, R., et al. 1984, ApJL, 278, L1
Nguyen, H. T., Schulz, B., Levenson, L., et al. 2010, A&A, 518, L5
North, D. O. 1943, Technical Report, RCA Laboratories, TR, PTR6C
Oteo, I., Ivison, R. J., Dunne, L., et al. 2016, ApJ, 827, 34
Ott, S. 2010, in Astronomical Society of the Pacific Conference Series, Vol. 434, Astronomical Data Analysis Software and Systems XIX, ed. Y. Mizumoto, K.-I. Morita, & M. Ohishi, 139
Pascale, E., Auld, R., Dariush, A., et al. 2011, MNRAS, 415, 911
Pearson, E. A., Eales, S., Dunne, L., et al. 2013, MNRAS, 435, 2753
Pilbratt, G. L., Riedinger, J. R., Passvogel, T., et al. 2010, A&A, 518, L1
Planck Collaboration, Ade, P. A. R., Aghanim, N., et al. 2011, A&A, 536, A1
Planck Collaboration, Adam, R., Ade, P. A. R., et al. 2016, A&A, 594, A1
Poglitsch, A., Waelkens, C., Geis, N., et al. 2010, A&A, 518, L2
Rigby, E. E., Maddox, S. J., Dunne, L., et al. 2011, MNRAS, 415, 2336
Robitaille, T., & Bressert, E. 2012, APLpy: Astronomical Plotting Library in Python, Astrophysics Source Code Library, , , ascl:1208.017
Roussel, H. 2013, PASP, 125, 1126
Shanks, T., Metcalfe, N., Chehade, B., et al. 2015, MNRAS, 451, 4238
Smith, D. J. B., Dunne, L., Maddox, S. J., et al. 2011, MNRAS, 416, 857
Smith, M. W. L. 2012, PhD thesis, Cardiff University
Thompson, M. A., Smith, D. J. B., Stevens, J. A., et al. 2010, A&A, 518, L134
Valiante, E., Smith, M. W. L., Eales, S., et al. 2016, MNRAS, 462, 3146
Van Der Walt, S., Colbert, S. C., & Varoquaux, G. 2011, IEEE CS & AIP, 13, 22
Viero, M. P., Moncelsi, L., Quadri, R. F., et al. 2013, ApJ, 779, 32
Waskett, T. J., Sibthorpe, B., Griffin, M. J., & Chanial, P. F. 2007, MNRAS, 381, 1583
Wright, E. L., Eisenhardt, P. R. M., Mainzer, A. K., et al. 2010, AJ, 140, 1868

APPENDIX

A. DATA RELEASE 2 PRODUCT INFORMATION

In this paper we described the *Herschel* images that form the second data release of *H*-ATLAS. All the data are available at www.h-atlas.org. A short description of each image released and the uses that they are optimized for are given in Table 5. In addition to the images listed in the table, we give the EEFs for each band, and a Multi-Order Coverage file (MOC, Fernique et al. 2014) which can be used to easily select the *H*-ATLAS region in other catalogs or maps. For SPIRE we also provide the PSFs and matched-filters used. The data release page also provides the *H*-ATLAS catalogs described in Maddox et al. (2017) and Furlanetto et al. (2017).

Table 5. Description and Uses of the Images Released

Instrument	Product Identifier	Map Unit	Processing Details	Optimised Use Cases
PACS	_BACKSUB	Jy pix^{-1}	Our released PACS images, created using the description in Section 4 and shown in Figure 3 & 5. These maps have been background subtracted with NEBULISER, which removes emission on scales above 300″.	Any flux density measurements with the PACS data should be made with these maps.
	_NSCAN	...	Image showing the number of individual observations that have contributed to the flux density in each pixel, as shown in Figure 3 & 5.	This image can be used to only select regions with a specific number of observations, and can be used together with with Table 4 to calculate sensitivity, or with Equation 6 to find the uncertainty on an aperture.
SPIRE	_RAW	Jy beam^{-1}	The raw SPIRE mosaic images, created using the description in Section 3.3 and shown in Figures 2 and 4.	Should be used in studies requiring large-scale structure to be preserved (i.e., cirrus emission, or large-angular size galaxies). This map can be used if the users wish to apply their own filtering methods.
	_BACKSUB	Jy beam^{-1}	The SPIRE maps that have been background subtracted using NEBULISER, which was set to remove emission scales greater than 30 pixels (equating to 3, 4 and 6′) at 250, 350, and 500μm, respectively (see Section 5.3).	This map is recommended for performing any aperture photometry or studies of extended sources (with the exception of very extended sources), and to perform a statistical stacking analysis (Viero et al. 2013).
	_FBACKSUB	Jy beam^{-1}	The point source optimized map, created by applying the matched-filter (see Section 3.3), to the background-subtracted map.	This map has been optimized for the detection and measurement of point sources. Any science goals investigating individual point sources should use this map.
	_NSCAN	...	Image showing the number of individual observations that have contributed to the flux density in each pixel, as shown in Figure 2 and 4.	This image can be used to only select regions with a specific number of observations, and can be used together with Table 1 to calculate sensitivity, or with Equation 4 to find the uncertainty on a flux measurement in an aperture.
	_MASK	...	A map showing the regions where the *H*-ATLAS source detection has been applied.	This map can be used to see whether a particular coordinate falls within the region covered by the *H*-ATLAS catalogue.
	_SIGMA	Jy beam^{-1}	The uncertainty map for our un-filtered SPIRE maps. The differences between this map and the default uncertainty maps produced by HIPE are described in Section 3.3.	This map can be used to find the instrumental noise for any pixel on the image. This is useful as the sensitivity can vary, even in regions with the same number of observations.
	_FSIGMA	Jy beam^{-1}	The uncertainty map for our matched-filtered maps (see Section 3.3).	This map can be used to find the instrumental noise for any pixel on the matched-filtered map. This is useful as the sensitivity can vary, even in regions with the same number of observations.

NOTE—The images released as part of *H*-ATLAS Data Release 2. The file names for the products in the table all include the field (NGP or SGP), the product identifier (column 2) and the wavelength in microns (100, 160, 250, 350, or 500).

B. CONFUSION INFORMATION

In Section 5.3 we recommended that for an individual source the confusion noise that is most appropriate to use is from our second definition in Section 5.2. In this method the confusion noise depends on the flux density of the source, and the relationship is shown in Figure 9. To allow users to use the most appropriate confusion value for their source, Table 6 provides the confusion noise values for each flux limit that was used to plot Figure 9.

Table 6. Confusion Noise versus Flux Limit

Flux Limit	Confusion Noise (mJy beam^{-1})											
	250μm				350μm				500μm			
	Raw		Nebulised		Raw		Nebulised		Raw		Nebulised	
(mJy beam^{-1})	NGP	SGP	NGP	SGP	NGP	SGP	NGP	SGP	NGP	SGP	NGP	SGP
0.0100	1.959	1.676	1.287	1.575	2.257	2.030	1.923	1.708	2.287	1.795	1.980	1.964
0.0126	2.063	2.051	1.967	1.700	2.727	2.598	2.362	2.272	2.708	2.455	2.352	2.130
0.0159	2.722	2.697	2.281	2.295	3.265	3.322	2.995	2.864	3.153	3.181	2.927	2.736
0.0200	3.282	3.273	2.954	2.941	4.120	4.011	3.573	3.582	3.965	3.919	3.470	3.568
0.0252	4.173	4.160	3.736	3.752	4.975	4.989	4.515	4.506	4.811	4.765	4.526	4.296
0.0317	4.973	4.998	4.621	4.519	5.856	5.845	5.475	5.385	5.690	5.639	5.405	5.158
0.0399	5.521	5.563	5.206	5.167	6.408	6.428	6.050	5.992	6.212	6.226	5.894	5.785
0.0502	5.870	5.925	5.580	5.551	6.720	6.755	6.375	6.338	6.487	6.492	6.115	6.064
0.0632	6.078	6.146	5.802	5.781	6.880	6.912	6.536	6.505	6.575	6.604	6.202	6.180
0.0796	6.221	6.293	5.962	5.937	6.958	6.990	6.620	6.593	6.616	6.638	6.234	6.208
0.1002	6.334	6.403	6.071	6.060	7.015	7.050	6.670	6.643	6.637	6.666	6.259	6.230
0.1262	6.427	6.495	6.168	6.151	7.064	7.093	6.727	6.684	6.661	6.686	6.276	6.261
0.1589	6.524	6.575	6.271	6.239	7.115	7.120	6.772	6.719	6.672	6.709	6.298	6.275
0.2000	6.624	6.656	6.366	6.326	7.164	7.151	6.816	6.756	6.690	6.735	6.315	6.302
0.2518	6.726	6.743	6.476	6.397	7.209	7.200	6.863	6.798	6.709	6.756	6.330	6.333
0.3170	6.844	6.813	6.582	6.482	7.250	7.244	6.903	6.840	6.728	6.787	6.344	6.339
0.3991	6.941	6.912	6.677	6.597	7.281	7.292	6.931	6.883	6.746	6.801	6.353	6.380
0.5024	7.024	7.038	6.770	6.710	7.308	7.333	6.955	6.948	6.747	6.833	6.363	6.403
0.6325	7.106	7.182	6.819	6.810	7.347	7.405	6.983	6.999	6.753	6.853	6.372	6.410
0.7962	7.162	7.290	6.892	6.900	7.356	7.440	7.004	7.049	6.757	6.864	6.378	6.438

NOTE—Estimates of the confusion noise in the three SPIRE bands using our second definition of confusion. Measurements are given for each field, and for both the raw and nebulised SPIRE maps.